Application of the multi-level time-harmonic fast multipole BEM to 3-D visco-elastodynamics

Eva Grasso, Stéphanie Chaillat, Marc Bonnet, Jean-François Semblat

To cite this version:

Eva Grasso, Stéphanie Chaillat, Marc Bonnet, Jean-François Semblat. Application of the multi-level time-harmonic fast multipole BEM to 3-D visco-elastodynamics. Engineering Analysis with Boundary Elements, 2012, 36, pp.744-758. 10.1016/j.enganabound.2011.11.015 . hal-00645208

HAL Id: hal-00645208

https://hal.science/hal-00645208

Submitted on 28 Nov 2011

Application of the multi-level time-harmonic fast multipole BEM to 3-D visco-elastodynamics

Eva Grasso[1,3], Stéphanie Chaillat[2], Marc Bonnet[2], Jean-François Semblat[3]

[1] LMS (UMR CNRS 7649), Ecole Polytechnique, Palaiseau, France (grasso@lms.polytechnique.fr)

[2] POems (UMR 7231 CNRS), Appl. Math. Dept., ENSTA, Paris, France ({marc.bonnet,stephanie.chaillat}@ensta.fr)

[3] Université Paris-Est, IFSTTAR, Paris, France (jean-francois.semblat@ifsttar.fr)

Abstract

This article extends previous work by the authors on the single- and multi-domain time-harmonic elastodynamic multi-level fast multipole BEM formulations to the case of weakly dissipative viscoelastic media. The underlying boundary integral equation and fast multipole formulations are formally identical to that of elastodynamics, except that the wavenumbers are complex-valued due to attenuation. Attention is focused on evaluating the multipole decomposition of the viscoelastodynamic fundamental solution. A damping-dependent modification of the selection rule for the multipole truncation parameter, required by the presence of complex wavenumbers, is proposed. It is empirically adjusted so as to maintain a constant accuracy over the damping range of interest in the approximation of the fundamental solution, and validated on numerical tests focusing on the evaluation of the latter. The proposed modification is then assessed on 3D single-region and multi-region visco-elastodynamic examples for which exact solutions are known. Finally, the multi-region formulation is applied to the problem of a wave propagating in a semi-infinite medium with a lossy semi-spherical inclusion (seismic wave in alluvial basin). These examples involve problem sizes of up to about $3\,10^5$ boundary unknowns.

1 INTRODUCTION

Elastic wave propagation in unbounded media is a useful idealization for a variety of real-life engineering problems, e.g. railway- or machinery-induced vibrations, seismic wave propagation, or soil-structure interaction. Various domain-based numerical methods, such as the finite difference method [1, 2], the finite element method [3, 4] and the spectral element method [5, 6] allow to solve elastic wave propagation in three-dimensional unbounded media. They however require the discretization of large 3D regions, leading after discretization to large systems of equations that easily involve millions of degrees of freedom and are prone to cumulative numerical dispersion. Moreover, to avoid the spurious reflected waves induced by artificially truncated domain boundaries, specific techniques such as absorbing boundary conditions [7, 8], the perfectly matched layers (PMLs) [9–11] or infinite elements [12] must be implemented. On the other hand, the Boundary Element method (BEM) [13, 14], in addition to the reduced model size allowed by the boundary-only discretization, is very well suited to dealing with propagation in unbounded media because of the built-in, exact satisfaction of radiation conditions.

However, solving the potentially large fully-populated non-symmetric linear system arising in the classical BEM formulation entails unreasonably high CPU time and memory requirements. The fast multipole algorithm is often applied to accelerate iterative solution algorithms applied to the global linear system of BEM equations [15]. The capabilities of the Fast Multipole-Boundary Element Method (FMBEM) and its recursive variant the Multi Level-FMBEM (ML-FMBEM) have rapidly progressed during the last decade, allowing many engineering applications requiring large BEM models, in connection with e.g. acoustics [16], elastodynamics [17], Stokes flows [18] or electromagnetism [19]. Fast BEMs have also been proposed using other approaches, in particular based on hierarchical matrices [20–22].

FMBEMs for real values of the wavenumber k, which correspond to wave propagation problems in undamped media, have been extensively studied and implemented, see e.g. [23–25] for background, while the collocation FMBEM for 3D-frequency domain elastodynamics in homogeneous or piecewise-homogeneous elastic media is addressed in [17, 26]. Importantly, these algorithms are backed by error analysis results for the multipole expansion of the fundamental solutions, which also provide guidelines about suitable settings of e.g. truncation parameters.

In contrast, only scattered efforts have so far been devoted to FMMs for Helmholtz-type problems involving complex wavenumbers of the form $k^{\star} = k(1 + \mathrm{i}\beta)$, with $\beta > 0$ quantifying material damping.

The overall FMBEM algorithm is identical to that for the corresponding lossless medium, but the setting of important algorithmic parameters such as the truncation parameter is affected by β, an issue which has not been studied in depth, in particular in terms of mathematical error analysis. A complex-wavenumber FMBEM formulation for electromagnetic scattering is proposed in [27, 28], where the truncation parameter is empirically shown to increase with β in order to maintain a given accuracy on the fundamental solution evaluation. Empirical studies on the low-frequency expansion [29] yield guidelines on the adjustment of the truncation parameter depending on β. The FMBEM analysis of sound fields in porous materials is addressed in [30], where contributions from cells located beyond a certain normalized distance from the evaluation point are simply ignored, resulting in a well-conditioned influence matrix and a reduced computational time. The latter approach is, however, not suitable for weakly dissipative media ($\beta \ll 1$) because the cut-off distance is proportional to β^{-1}.

This work is concerned with carrying over the single- and multi-domain elastodynamic FMBEM formulations of [17, 26] to the case of weakly dissipative viscoelastic media. Indeed, the ability to consider material attenuation enables more realistic wave propagation modelling, allowing to e.g. reproduce the amplitude decay of propagating waves or free vibrations or describe the finite amplitudes and phase shifts of systems excited near resonance [31]. This article is organized as follows. Section 2 gathers necessary background about the time-harmonic behavior of weakly dissipative viscoelastic media, the relevant BIE formulation and its solution using the ML-FMBEM. Section 3 then concentrates on the crucial task of evaluating the multipole decomposition of the viscoelastodynamic fundamental solution, where a damping-dependent modification of the selection rule for the multipole truncation parameter, required by the presence of complex wavenumbers, is proposed, empirically adjusted so as to maintain a constant accuracy over the damping range of interest in the approximation of the fundamental solution, and validated on numerical tests focusing on the evaluation of the latter. The proposed modification is next assessed in Sec. 4 on full visco-elastodynamic examples for which an exact solution is known. In Sec. 5, the visco-elastodynamic settings are finally applied to the multi-domain version of the ML-FMBEM featuring a BE-BE coupling strategy, previously developed in [17] for the elastodynamic case, and validated on a simple spherically-symmetric configuration and on the problem of a wave propagating in a semi-infinite medium with a lossy semi-spherical inclusion (seismic wave in alluvial basin).

2 MULTI-LEVEL FM-BEM FORMULATION FOR 3D VISCOELASTODYNAMICS

2.1 The time-harmonic dynamics of viscoelastic media

Experimental evidence shows that strains below the so-called *linear cyclic threshold strain* correspond to a nearly linear material response, whereas at larger strains non-linear behavior sets in and eventually dominates. The intended applications of this work are seismic or traffic-induced wave propagation, for which shear strain levels are below the linear threshold. In this range, the soil behavior is accurately described, from the phenomenological point of view, by the theory of linear viscoelasticity.

Constitutive law for an isotropic linear viscoelastic medium. The constitutive relation for a linear viscoelastic medium is given by [32]

$$\sigma_{ij}(\mathbf{x},t) = \int_{-\infty}^{t} \mathcal{C}_{ijk\ell}(t-\tau)\,\dot{\varepsilon}_{k\ell}(\mathbf{x},\tau)d\tau, \tag{1}$$

where $\sigma_{ij}(\mathbf{x},t)$ and $\varepsilon_{k\ell}(\mathbf{x},\tau)$ are generic components of the stress and linearized strain tensors and $\mathcal{C}_{ijk\ell}$ is the relaxation tensor. For an homogeneous isotropic viscoelastic medium, the relaxation tensor is written in terms of two independent Lamé-type coefficients

$$\mathcal{C}_{ijk\ell}(t) = \big[\lambda(t)\delta_{ij}\delta_{k\ell} + \mu(t)(\delta_{ik}\delta_{j\ell} + \delta_{i\ell}\delta_{jk})\big]H(t), \tag{2}$$

where $H(\cdot)$ is the Heaviside step function. In this article, time-harmonic motions with angular frequency ω are considered, and the strain then takes the form $\varepsilon_{ij}(\mathbf{x},\tau) = \varepsilon_{ij}(\mathbf{x})e^{-\mathrm{i}\omega\tau}$; a similar behavior is assumed for all other time-varying quantities. Eq. (1) then becomes [33]

$$\sigma_{ij}(\mathbf{x},t) = \left[\mathrm{i}\omega\int_{-\infty}^{\infty}\lambda(\eta)H(\eta)e^{\mathrm{i}\omega\eta}d\eta\right]\varepsilon_{kk}(\mathbf{x})\delta_{ij}e^{-\mathrm{i}\omega t} + 2\left[\mathrm{i}\omega\int_{-\infty}^{\infty}\mu(\eta)H(\eta)e^{\mathrm{i}\omega\eta}d\eta\right]\varepsilon_{ij}(\mathbf{x})e^{-\mathrm{i}\omega t},$$

having used the transformation $\eta := t - \tau$ and with the zero lower bound of the integral replaced by $-\infty$ by virtue of (2). The terms inside square brackets are the Fourier transforms $\lambda^\star(\omega)$ of $\lambda(t)H(t)$ and $\mu^\star(\omega)$ of $\mu(t)H(t)$, respectively. With the time factor $e^{-\mathrm{i}\omega\tau}$ omitted hereon, the constitutive relation (1) is finally written in the form

$$\sigma_{ij}(\mathbf{x},\omega) = \mathcal{C}^\star_{ijk\ell}(\omega)\varepsilon_{k\ell}(\mathbf{x},\omega), \qquad \mathcal{C}^\star_{ijk\ell}(\omega) = \lambda^\star(\omega)\delta_{ij}\delta_{k\ell} + \mu^\star(\omega)(\delta_{ik}\delta_{j\ell} + \delta_{i\ell}\delta_{jk}), \tag{3}$$

which emphasizes the well-known formal analogy between linear viscoelastic and linear elastic time-harmonic problems, the main difference between the two situations being that the Lamé coefficients, wave velocities and wavenumbers are complex-valued and frequency-dependent in the viscoelastic case (in which case an asterisk is used, in (3) and hereinafter, to distinguish them from their real-valued, elastic, counterparts). For the present work, carried out in the frequency domain, the dependence of the material damping on the frequency does not play a significant role, whereas time-domain analyses would require an appropriate theoretical or empirical model for the lossy medium (soil), e.g. a rheological model, which takes into account the attenuation-frequency dependence [34, 35].

Complex wavenumbers and mechanical parameters for weakly dissipative media. Complex wavenumbers $k^\star$ have the form [34, 36]

$$(k^\star(\omega))^2 = \rho\omega^2/M^\star(\omega) \tag{4}$$

(where $M^\star(\omega) = M_r(\omega) - \mathrm{i}M_i(\omega)$, with $M_r > 0$ and $M_i \geq 0$, is a complex modulus (e.g. $M^\star = \lambda^\star$ or $\mu^\star$) and $|M^\star(\omega)| = \sqrt{M_r^2(\omega) + M_i^2(\omega)}$ its absolute value), and may be written as

$$k^\star(\omega) = k(\omega)[1 + \mathrm{i}\beta(\omega)], \tag{5}$$

where $k(\omega)$ (the real wavenumber) and $\beta(\omega)$ (the material damping ratio) are given by [37]:

$$k(\omega) = \omega\sqrt{\frac{\rho(|M^\star| + M_r)}{2|M^\star|^2}}, \qquad \beta(\omega) = \sqrt{\frac{|M^\star| - M_r}{|M^\star| + M_r}}. \tag{6}$$

The material damping parameter β is mostly used in geotechnical earthquake engineering. Damping is equivalently quantified using the loss factor $\eta = 2\beta$ (in structural dynamics and vibration analysis), or the attenuation $Q^{-1} = 2\beta$ (in seismology [38] or acoustics [34]); all these parameters are clearly dimensionless.

In the case of weakly dissipative media, i.e. $|M_i| \ll M_r$, a Taylor expansion of $\beta(\omega)$ in powers of $\zeta(\omega) := M_i(\omega)/M_r(\omega)$ yields

$$\beta(\omega) = \zeta(\omega)/2 + o(\zeta(\omega)) \tag{7}$$

Damping in real soils follows the weak-dissipation assumption, with typical values in the range $\beta = 0.03 - 0.06$. The complex-valued Lamé constants can then be written as [33]:

$$\mu^\star = \mu(1 - 2\mathrm{i}\beta_\mu) + o(\beta_\mu), \qquad \lambda^\star = \lambda(1 - 2\mathrm{i}\beta_\lambda) + o(\beta_\lambda)$$

in terms of the distinct material damping ratios β_μ, β_λ which allow to distinguish the contribution to the damping of shear and pressure waves. The complex shear wavenumber is hence given by $k^\star_S = k_S(1+\mathrm{i}\beta_\mu)$, where $k_S = \omega\sqrt{\rho/\mu}$ is the real shear wavenumber. The complex pressure wavenumber $k^\star_P$, the complex Poisson's ratio $\nu^\star$ and the complex S- and P-wave velocities are then given by:

$$k^\star_P = k^\star_S\gamma^\star, \qquad \nu^\star = \lambda^\star \,/\, (2\lambda^\star + 2\mu^\star), \qquad c^\star_S = \sqrt{\mu^\star/\rho} \qquad \text{et} \quad c^\star_P = c^\star_S/\gamma^\star, \tag{8}$$

with $\gamma^{\star 2} = \mu^\star/(\lambda^\star + 2\mu^\star) = (1 - 2\nu^\star)/(2(1 - \nu^\star))$. For the sake of simplicity, the material damping ratios are assumed to be the same, i.e. $\beta = \beta_\mu = \beta_\lambda$, in the remainder of this article. The complex Poisson's ratio then reduces to the real Poisson's ratio, i.e. $\nu^\star = \nu = \lambda/2(\lambda + \mu)$.

2.2 Viscoelastodynamic boundary element formulation

Let $\Omega \subset \mathbb{R}^3$ denote a region of space occupied by a three-dimensional isotropic homogeneous viscoelastic solid. Assuming the absence of body forces, the displacement u is given at an interior point $\mathbf{x} \in \Omega$ by the classical boundary integral representation formula

$$u_k(\mathbf{x}) = \int_{\partial\Omega} \big[t_i(\mathbf{y})U^k_i(\mathbf{y}-\mathbf{x};\omega) - u_i(\mathbf{y})T^k_i(\mathbf{x},\mathbf{y};\omega)\big]\, dS_y \qquad (\mathbf{x} \in \Omega), \tag{9}$$

where $\mathbf{t}$ is the traction vector. $U_i^k(\mathbf{y}–\mathbf{x};\omega)$ and $T_i^k(\mathbf{x},\mathbf{y};\omega)$ denote the $i-$th components of the displacement and traction vector associated to the visco-elastodynamic fundamental solution generated at a point $\mathbf{y}\in\mathbb{R}^3$ by a unit point force applied at $\mathbf{x}\in\mathbb{R}^3$ along the direction k, given by [39]

$$\begin{aligned} U_i^k(\mathbf{y}-\mathbf{x};\omega) &= \frac{1}{k_S^{\star 2}\mu^\star}\left((\delta_{qs}\delta_{ik}-\delta_{qk}\delta_{is})\frac{\partial}{\partial x_q}\frac{\partial}{\partial y_s}G(\|\mathbf{y}-\mathbf{x}\|;k_S^\star)+\frac{\partial}{\partial x_i}\frac{\partial}{\partial y_k}G(\|\mathbf{y}-\mathbf{x}\|;k_P^\star)\right) \\ T_i^k(\mathbf{x},\mathbf{y};\omega) &= \mathcal{C}^\star_{ijh\ell}(\omega)\frac{\partial}{\partial y_l}U_h^k(\mathbf{y}-\mathbf{x};\omega)n_j(\mathbf{y}), \end{aligned} \tag{10}$$

in terms of the free-space Green's function for the Helmholtz equation

$$G(r;k^\star)=\frac{e^{ik^\star r}}{4\pi r}=e^{-\beta kr}\frac{e^{ikr}}{4\pi r}, \tag{11}$$

and where $\mathbf{n}(\mathbf{y})$ is the outward unit normal and the relaxation tensor components $\mathcal{C}^\star_{ijh\ell}$ are given by (3). In (11), waves emitted by a source point $\mathbf{x}$ are spatially oscillatory, which is reflected by the real wavenumber k, while also exponentially decaying away from $\mathbf{x}$ when material damping is present, i.e. $\beta>0$.

Assuming Neumann boundary conditions for definiteness, the limiting case $\mathbf{x}\in\partial\Omega$ in the integral representation (9) yields the singular boundary integral equation (BIE) [13, 14]:

$$(\mathcal{K}u)(\mathbf{x})=f(\mathbf{x}) \qquad (\mathbf{x}\in\partial\Omega), \tag{12}$$

with the linear operator $\mathcal{K}$ and the right-hand side f given by

$$\begin{aligned} (\mathcal{K}u)(\mathbf{x}) &= c_{ik}(\mathbf{x})u_i(\mathbf{x})+(\text{P.V.})\int_{\partial\Omega}u_i(\mathbf{y})T_i^k(\mathbf{x},\mathbf{y};\omega)dS_y \\ f(\mathbf{x}) &= \int_{\partial\Omega}t_i^D(\mathbf{y})U_i^k(\mathbf{x},\mathbf{y};\omega)dS_y \qquad (\mathbf{x}\in\partial\Omega). \end{aligned}$$

where (P.V.) indicates a Cauchy principal value (CPV) singular integral. The free-term $c_{ik}(\mathbf{x})$ depends on the local boundary geometry and it is equal to $\delta_{ik}/2$ at any smooth boundary point $\mathbf{x}\in\partial\Omega$.

The numerical solution of BIE (12) is based on a discretization of the surface $\partial\Omega$ into N_E isoparametric boundary elements, with piecewise-linear interpolation of displacements, based on three-noded triangular boundary elements, used in this work. The N_I displacement interpolation nodes thus defined also serve as collocation points. A square complex-valued matrix equation of size $N=3N_I$ of the form

$$\mathbb{K}\mathbb{U}=\mathbb{F}, \tag{13}$$

is obtained, where (i) $\mathbb{U}\in\mathbb{C}^N$ collects the unknown nodal displacement components and (ii) $\mathbb{K}\in\mathbb{C}^{N\times N}$ (influence matrix) and $\mathbb{F}\in\mathbb{C}^N$ are discrete versions of $\mathcal{K}$ and f, respectively. Setting up $\mathbb{K}$ classically entails computing all element integrals for each collocation point, at a $\mathcal{O}(N^2)$ computational cost.

2.3 Multi-Level Fast Multipole BEM (ML-FMBEM)

The fully-populated nature of $\mathbb{K}$ makes both its storage and the application of direct solvers either impractical or impossible for BEM model sizes exceeding $N=\mathcal{O}(10^4)$. Instead, iterative solvers such as GMRES [40] must be used, but large BEM models require that integral operators (i.e., after discretization, matrix-vector products $\mathbb{K}\mathbb{U}$) be evaluated using procedures which are faster than the standard method, whose $\mathcal{O}(N^2)$ complexity is prohibitive. A widely used approach for that purpose is the fast multipole method (FMM), based on a reformulation of the fundamental solutions in terms of products of functions of $\mathbf{x}$ and $\mathbf{y}$. This allows to re-use integrations with respect to $\mathbf{y}$ when the collocation point $\mathbf{x}$ is changed, and thus to lower the overall complexity (to $\mathcal{O}(N\log N)$ using the multi-level form of the FMM).

The main features of the fast multipole BEM (FMBEM) formulation considered are those previously developed in [26] for the elastodynamic (i.e. non-dissipative) case, based on the decomposition of $G(r;k)$ in diagonal form [15, 41, 42]. The latter, which rests upon choosing two poles $\mathbf{x}_0,\mathbf{y}_0$ respectively close to $\mathbf{x},\mathbf{y}$, recasting the position vector $\mathbf{r}=\mathbf{y}–\mathbf{x}$ as $\mathbf{r}=(\mathbf{y}–\mathbf{y}_0)+\mathbf{r}_0+(\mathbf{x}_0–\mathbf{x})=\mathbf{r}_0+\mathbf{r}'$ (Fig. 1) and invoking the Gegenbauer addition theorem (see [25] and [43] formulae 10.1.45 and 10.1.46), reads:

$$G(r;k^\star)=\lim_{L\to+\infty}G_L(r;k^\star), \qquad G_L(r;k^\star):=\int_{\hat{\mathbf{s}}\in\mathcal{S}}e^{\mathrm{i}k^\star\hat{\mathbf{s}}.(\mathbf{y}-\mathbf{y}_0)}\mathcal{G}_L(\hat{\mathbf{s}};\mathbf{r}_0;k^\star)e^{\mathrm{i}k^\star\hat{\mathbf{s}}.(\mathbf{x}_0-\mathbf{x})}d\hat{\mathbf{s}} \tag{14}$$

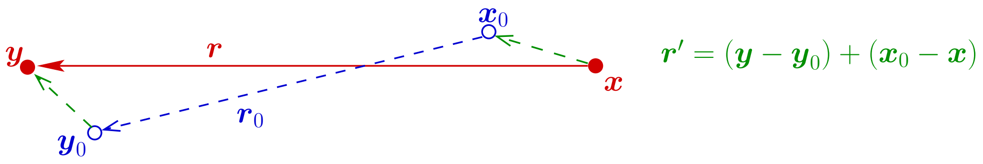

Figure 1: *Plane wave expansion of the Helmholtz Green's function: decomposition of the position vector.*

where $\mathcal{S} = \left\{\hat{\mathbf{s}} \in \mathbb{R}^3,\ \|\hat{\mathbf{s}}\| = 1\right\}$ is the unit sphere and the transfer function $\mathcal{G}_L(\hat{\mathbf{s}}; \mathbf{r}_0; k^\star)$ is given by

$$\mathcal{G}_L(\hat{\mathbf{s}}; \mathbf{r}_0; k^\star) = \frac{ik^\star}{16\pi^2} \sum_{\ell=1}^{L} (2\ell+1) i^\ell h_\ell^{(1)}(k^\star r_0) P_\ell(\hat{\mathbf{s}}.\hat{\mathbf{r}}_0), \tag{15}$$

in terms of the spherical Hankel functions of first kind $h_\ell^{(1)}$ and Legendre polynomials P_ℓ, and with $\hat{\mathbf{r}}_0 = \mathbf{r}_0/r_0$. Equation (14) essentially represents G as a superposition of plane waves. A key error analysis result for the real-wavenumber case [25] states that, if $\mathbf{x}_0, \mathbf{y}_0$ are chosen so as to have

$$r'/r_0 \leq 2/\sqrt{5} \qquad (r' := \|\mathbf{r}'\|,\ r_0 := \|\mathbf{r}_0\|) \tag{16}$$

there exist four constants C_1, C_2, C_3, C_4 such that for given $\epsilon < 1$, one has $|G_L(r; k) - G(r; k)| < \epsilon$ if [25]

$$L(r') = C_1 + C_2 kr' + C_3 \ln(kr') + C_4 \ln(\epsilon^{-1}). \tag{17}$$

The multi-level FM-BEM exploits a recursive subdivision of a cube enclosing the domain Ω (level 0) into 8 cubic cells (levels 1, , 2 . . .), see Fig. 2. The subdivision process stops when the linear size of the smallest cells becomes smaller than the threshold $d_{\text{min}} = \alpha\lambda_S$ corresponding to a certain preset fraction α of the shear wavelength λ_S. The deepest level $\bar{\ell}$ reached in the subdivision process, termed the *leaf level*, is such that $d^{(\bar{\ell}+1)} \leq d_{\text{min}} \leq d^{(\bar{\ell})}$. The presence of a lower threshold d_{min} is due to the divergent behavior of $h_n^{(1)}(z)$ in the small-argument limit, entailing a loss of accuracy when using small cell sizes. The cell size threshold α has to be estimated through numerical tests. The value $\alpha = 0.3$ was found to be suitable in the elastodynamic case [26].

In this hierarchical structure, $\mathbf{x}_0$ and $\mathbf{y}_0$ in (14) are chosen as the centers of two cubic cells. For two cells that are not adjacent (i.e. that do not even share a corner), one always has $r'/r_0 \leq \sqrt{3}/2$. Partitioning the space into cubic cells thus ensures verification of condition (16), and hence convergence

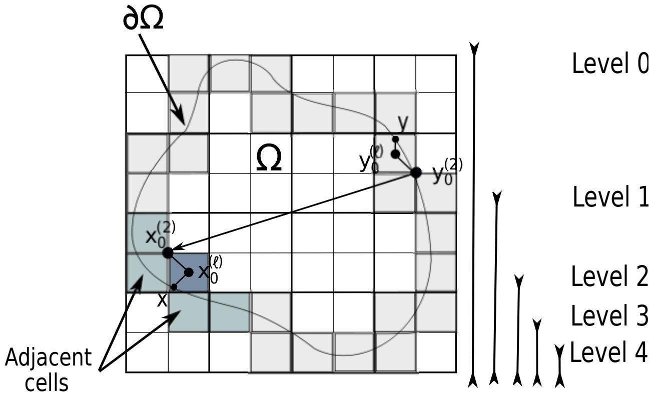

Figure 2: *Sketch of the ML-FMBEM. For a given collocation point $\mathbf{x}$, far field contributions from points $\boldsymbol{y}$ belonging to non-adjacent cells are gathered at $\boldsymbol{y}_0^{(\bar{\ell})}$, accumulated upwards at all parent cell centers up to $\boldsymbol{y}_0^{(2)}$, transferred to same-level non-adjacent cell centers $\mathbf{x}_0^{(2)}$ belonging to the interaction list of $\boldsymbol{y}_0^{(2)}$, accumulated downwards in all children cells down to $\mathbf{x}_0^{(\bar{\ell})}$, and finally locally expanded at $\mathbf{x}$ about $\mathbf{x}_0^{(\bar{\ell})}$.*

of (14) for $L \to +\infty$, whenever the collocation points $\mathbf{x}$ and the integration points $\mathbf{y}$ lie in non-adjacent cells. The highest active level is $\ell = 2$, as pairs of non-adjacent cells cannot occur at levels 0 or 1. The multi-level FMBEM exploits the representation (14) to evaluate the influence of far integration points $\mathbf{y}$ clustered around $\mathbf{y}_0$ on the collocation points $\mathbf{x}$ clustered around $\mathbf{x}_0$, $\mathbf{y}_0$ and $\mathbf{x}_0$ being the center of non-adjacent clusters. The influence matrix $\mathbb{K}$ is then additively split into two parts. The part $\mathbb{K}^{\text{near}}$ containing the contributions from adjacent cells, which is sparse, is set up (using usual BEM integration and assembly techniques) and stored. The contribution $\mathbb{K}^{\text{FM}}$ exploiting the expansion (14) is neither set up nor stored. Instead, the contribution $\mathbb{K}^{\text{FM}}\mathbb{U}$ to the matrix-vector product $\mathbb{K}\mathbb{U}$ is computed for each GMRES iteration. Summarizing, the acceleration introduced by the FM algorithm rests on (i) the reduction of the integrations on $\partial\Omega$ coming from the separation of variables introduced in (14), and (ii) the optimal tasks partitioning allowed by the recursive subdivision.

Truncation of the transfer function. The multipole expansion (14) is convergent in the limit $L \to +\infty$ allowing the convergence of the viscoelastodynamic kernels. However, for computational reasons, it is evaluated for a finite value of the truncation parameter L, and the FMBEM uses the truncated approximation $G_L(r; k^\star)$ of $G(r; k^\star)$. Choosing a suitable truncation level L is delicate, as L has to be large enough to guarantee sufficient accuracy in (14), while not exceeding values significantly larger than $k^\star r$ so as to avoid blow-up of the Hankel functions $h_n^{(1)}$ occurring for $n \gg z$.

Besides its influence on the convergence of (14), the parameter L affects both computational time and memory consumption. Indeed, the numerical integration over the unit sphere $\mathcal{S}$ is based on a product rule in the angular spherical coordinates (θ, ϕ) which needs $\mathcal{O}(L^2)$ points overall [42], since the polar coordinate $\theta \in [0, \pi]$ and the azimuthal coordinate $\phi \in [0, 2\pi]$ are treated using a $(L+1)$-point Gaussian rule and a $2L$-point uniform rule, respectively. This approach allows to integrate exactly the $L^2(\mathcal{S})$-orthonormal set of spherical harmonics $(Y_{p,m}(\theta, \phi))_{0 \le p \le L, -p \le m \le p}$ of order $\le L$.

The choice of the parameter L is thus critical for both the performance and the efficiency of the FMBEM algorithm. In real-wavenumber problems, L is set according to a rule involving kD (with D the length of the cell diagonal), and is thus level-dependent as a result. In particular, for an accurate evaluation of decomposition (14), L must be slightly greater than kD [44].

In practice, selecting the truncation parameter L using rules inspired by (17) requires adjusting the constants using numerical experiments [45, 46]. In elastodynamics, starting from a relation of the form

$$L_{\text{E}}(D; C) = kD + C \log_{10}(kD + \pi), \tag{18}$$

the constant C has been empirically set to $C = 7.5$, by seeking a trade-off between the RMS discrepancy between ML-FMBEM versus standard BEM and the CPU time per iteration [26]. Relation (18) depends on the cell linear size D through the dimensionless parameter $k|\mathbf{r}'|$, hence is level-dependent.

3 TRUNCATION OF THE TRANSFER FUNCTION WITH COMPLEX WAVENUMBER

This section is concerned with the numerical evaluation of the plane-wave decomposition (14) when using complex wavenumbers, so as to determine practical settings for the visco-elastodynamic ML-FMBEM exploiting that representation of the fundamental solution.

3.1 Evaluation of the transfer function

The viscoelastic constitutive parameters of the medium, e.g. the wave velocities and wavenumbers, are complex-valued and frequency-dependent (Sec. 2.1). This is expected to affect the ML-FMBEM mainly through the setting of L for the evaluation of the kernel approximation (14). The latter, after replacing the integral over the unit sphere $\mathcal{S}$ by a discrete quadrature with points $\hat{\mathbf{s}}_q \in \mathcal{S}$ and weights w_q, reads:

$$G(r; k^\star) \sim \sum_{q=1}^{Q} w_q e^{ik^\star(\hat{\mathbf{s}}_q \cdot \mathbf{r}')} \mathcal{G}_L(\hat{\mathbf{s}}_q; \mathbf{r}_0; k^\star). \tag{19}$$

In general, the error induced by using decomposition (14) for a finite value of L and replacing the integration over $\mathcal{S}$ by the discrete numerical quadrature (featuring $Q = \mathcal{O}(L^2)$ points) depends on $\mathbf{r}'$

(position of points $\mathbf{x},\mathbf{y}$ with respect to local poles $\mathbf{x}_0,\mathbf{y}_0$), $|k^\star D|$ (dimensionless cell size), r_0 (distance between cells) and on the choice of quadrature rule. At any given level, the most unfavorable configuration, leading to the least accurate evaluation of $G(r;k^\star)$, corresponds to non-adjacent cells that are closest (Fig. 3). This particular configuration has been considered as a reference configuration in the following.

Empirical observations in the real-wavenumber case ($k^\star = k$, $\beta = 0$). When r_0 increases, the approximation $G_L(r;k^{)}$ of $G(r;k)$ becomes more accurate, as shown in Fig. 4(a-c), where the relative error $\varepsilon = |G_L - G|/|G|$ is depicted as a function of kd and L for three different relative distances between cells $r_0 = 2d$, $2D$ and $3D$ (Fig. 4, top left), d being the linear cell size and $D = \sqrt{3}d$ the cell diagonal. When r' increases, i.e. the points $\mathbf{x},\mathbf{y}$ move farther from poles $\mathbf{x}_0,\mathbf{y}_0$, the exponential in (19) oscillates, reducing the accuracy of G_L, see Fig. 5.

Loss of accuracy of the multipole expansion in the damped case. For a given configuration of cells and points, increasing values of the damping ratio β leads to a loss of accuracy in the evaluation of $G(r;k^\star)$. This is shown in Fig. 6 for two points $\mathbf{x},\mathbf{y}$ lying in a pair of closest non-adjacent cells and such that $r' = 0.8D$. The behavior of the spherical Hankel functions with complex arguments influences the computation of the transfer operator (15); it is addressed in [47, 48]. The classical ascending three-

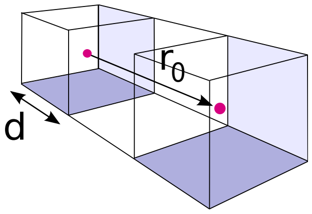

Figure 3: *Closest non-adjacent cells ($r_0 = 2d$), for which G_L yields a least accurate approximation of G.*

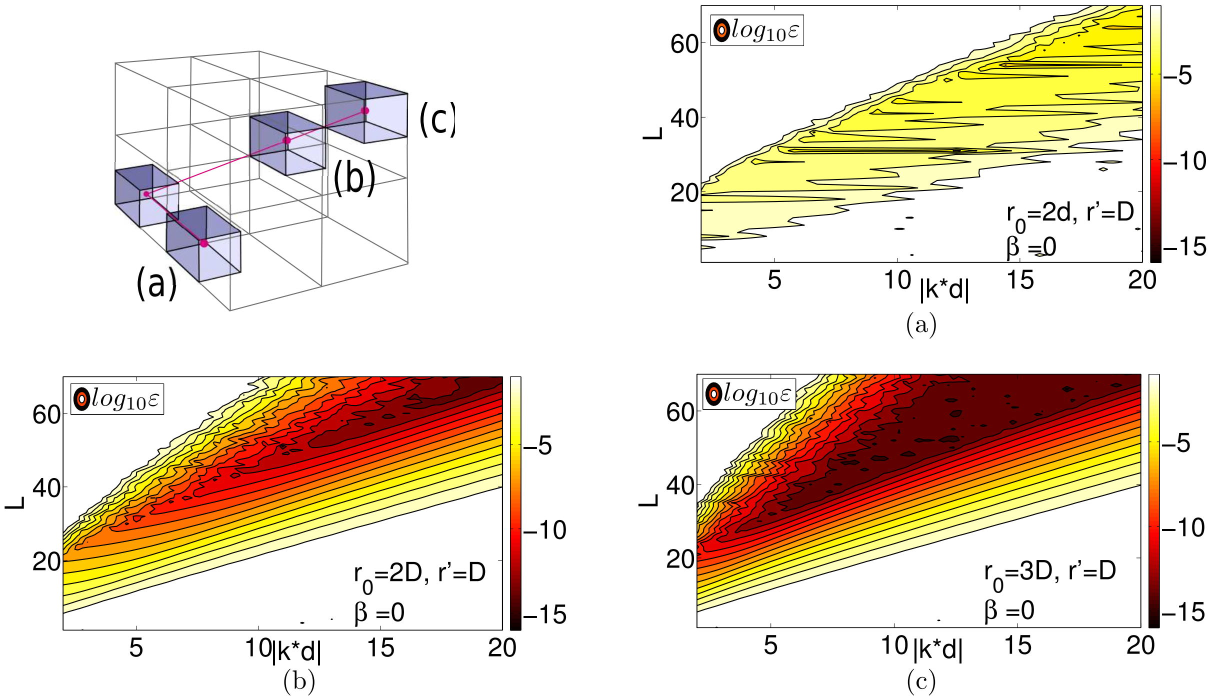

(a)

(b)

(c)

Figure 4: *Influence of the distance between cells $\mathbf{r}_0$ on the accuracy of the multipole expansion: contour lines of $log_{10}(\varepsilon)$. $\mathbf{x}$ and $\mathbf{y}$ are located at a fixed distance $r' = D$.*

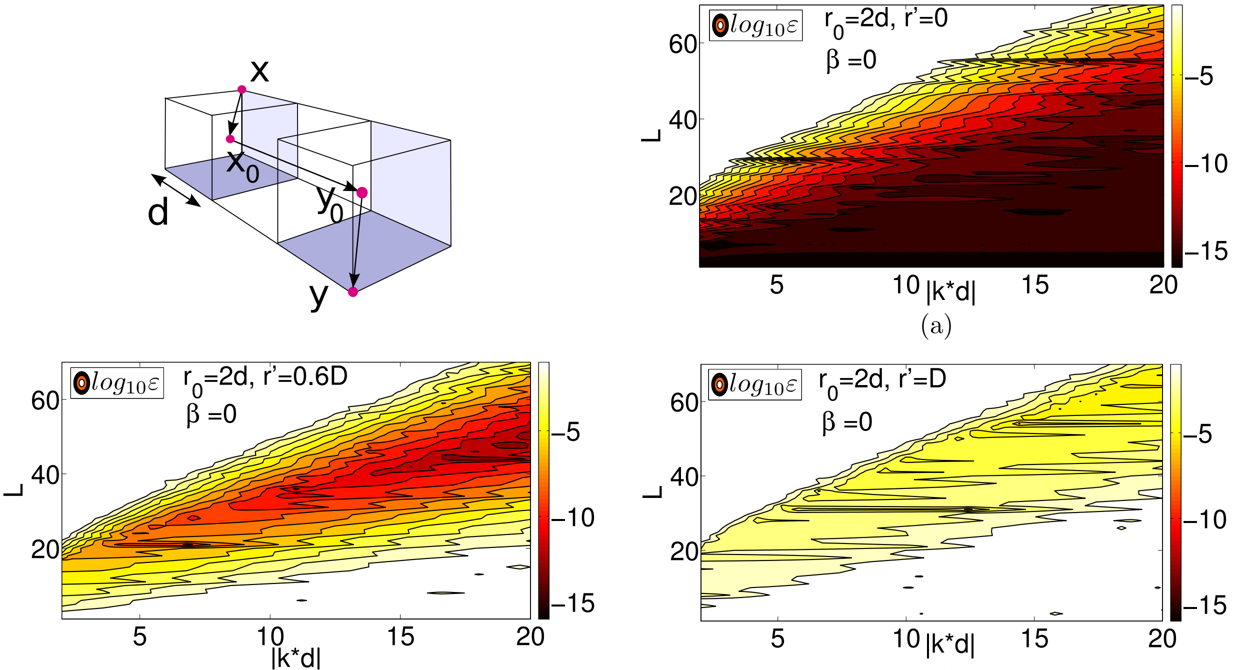

(a)

(b)

(c)

Figure 5: *Influence of r' on the accuracy of expansion (14): contour lines of $log_{10}\varepsilon$ (a) $r' = 0$, i.e. $\mathbf{x} = \mathbf{x}_0$, $\mathbf{y} = \mathbf{y}_0$; (b) $r' = 0.6D$; (c) $r' = D$, i.e. $\mathbf{x}, \mathbf{y}$ lie on opposite vertices.*

term recurrence (TTR) formula [43] is stable and can be employed for the evaluation of $h_n^{(1)}(k^\star r_0)$ with ascending n. The value of L defined by equation (18) becomes suboptimal for $\beta > 0$ and needs to be adjusted as a function of β. To study the error due to the choice of L on the approximation $G_L(k^\star, |\mathbf{r}_0 + \mathbf{r}'|)$ of $G(k^\star, r)$, a relative error ξ has been defined for the most unfavorable cell configuration ($r_0 = 2d$) in the form:

$$\xi^2(\beta) = \Big(\sum_{|k^\star d|}\sum_{r'} |G - G_L|^2\Big) \Big/ \Big(\sum_{|k^\star d|}\sum_{r'} |G|^2\Big). \tag{20}$$

Mesh nodes or quadrature points may lie anywhere in a cell. Thus, to obtain a realistic set of points inside a cell, uniform and Gaussian distributions have been considered for $\mathbf{r}'$. The error $\xi(\beta)$ is depicted in Fig. 7 (solid lines) for one distribution of $\mathbf{r}'$ of each type. Although $\xi(\beta)$ is lower for the Gaussian distribution, the accuracy in the evaluation of $G(k^\star, r)$ for both distributions progressively deteriorates as β increases. In the following, we propose to modify the selection rule (18) by making it dependent on β so as to achieve a constant average accuracy ξ over the damping range $0 \le \beta \le 0.1$ representative of weakly dissipative materials.

3.2 New damping-dependent selection rule for truncation parameter L

Having shown in section 3.1 that selecting L according to (18) does not guarantee that G_L given by (14) approximates G sufficiently well in the complex-wavenumber case, a modified selection rule that depends on the damping level β, where $L_{\text{E}}(D; C)$ defined by (18) is replaced by $L_{\text{V}}(D; \beta, C_1, C_2)$ defined by

$$L_{\text{V}}(D; \beta, C_1, C_2) = k^\star D + (7.5 + C_1\beta)\log_{10}(k^\star D + \pi) + C_2\beta, \tag{21}$$

is now considered. Note that (18) is a special case of (21), since $L_{\text{V}}(D; 0, 0, 0) = L_{\text{E}}(D)$, and that the influence of β on the selection rule is controlled by the adjustable constants C_1, C_2. The relative error indicator (20) has accordingly be redefined so as to perform an averaging over the damping range

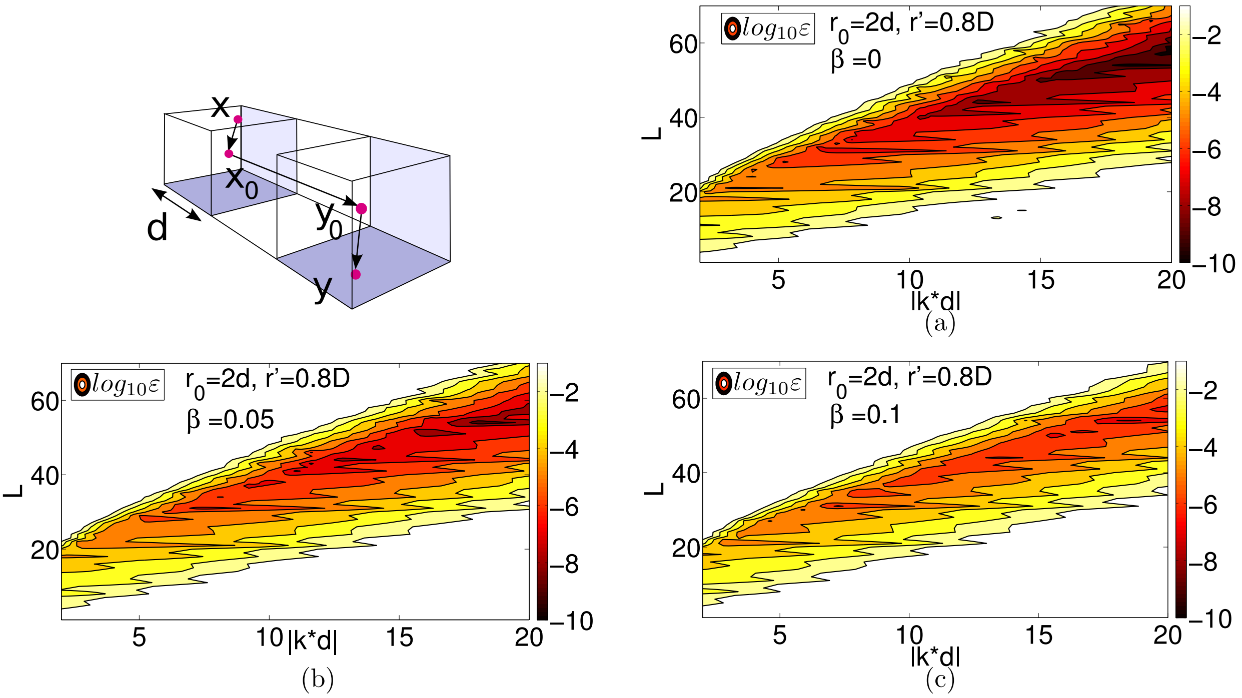

Figure 6: *Influence of β on the accuracy of expansion* (14)*: contour lines of $\log_{10}\varepsilon$ for two given points belonging to the closest non-adjacent cells ($r_0 = 2d$) at a fixed distance from poles ($r' = 0.8D$).*

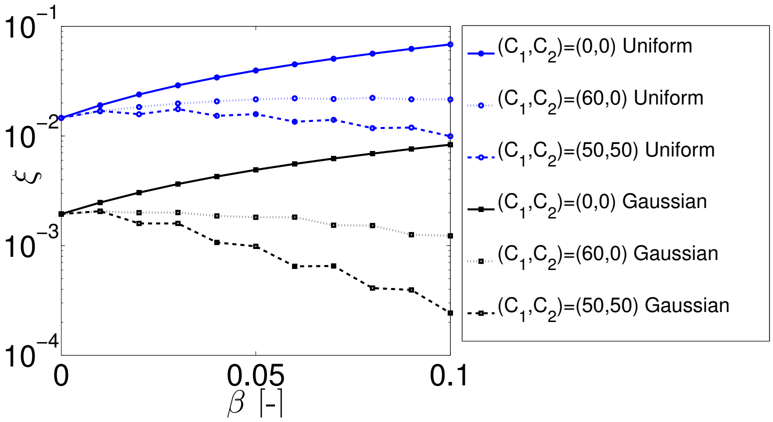

Figure 7: *Relative error ξ in the numerical evaluation of expansion* (14)*: influence of β and constants C_1, C_2, for two assumed distributions of $\mathbf{r}'$, with $r_0 = 2d$ fixed.*

$0 \leq \beta \leq 0.1$:

$$\zeta^2(C_1, C_2) = \left(\sum_{\beta} \sum_{|k^\star d|} \sum_{r'} \left| G - G_L \right|^2 \right) \Big/ \left(\sum_{\beta} \sum_{|k^\star d|} \sum_{r'} |G|^2 \right). \tag{22}$$

Suitable settings of C_1, C_2 are now sought from empirical tests. Figure 8 shows the contour lines of $\zeta(C_1, C_2)$ for $0 \leq C_1, C_2 \leq 50$ (blue lines) and the value of $L_{\mathrm{V}}(D; \beta, C_1, C_2)$ (red lines). As $C_1, C_2 > 0$ increase, the value of L increases while decomposition (14) approximates G better. Many combinations of C_1, C_2 thus achieve a given error level ζ. Among these, setting $C_2 = 0$ and using a nonzero value for C_1 is seen to correspond to the lowest value of L, i.e. it is cheapest in terms of CPU time. This required reformulating the adjustment rule for L in terms of a new function L'_{V}, with

$$L'_{\mathrm{V}}(D; \beta, C) = k^\star D + (7.5 + C\beta) \log_{10}(k^\star D + \pi) = L_{\mathrm{V}}(D; \beta, C, 0) \tag{23}$$

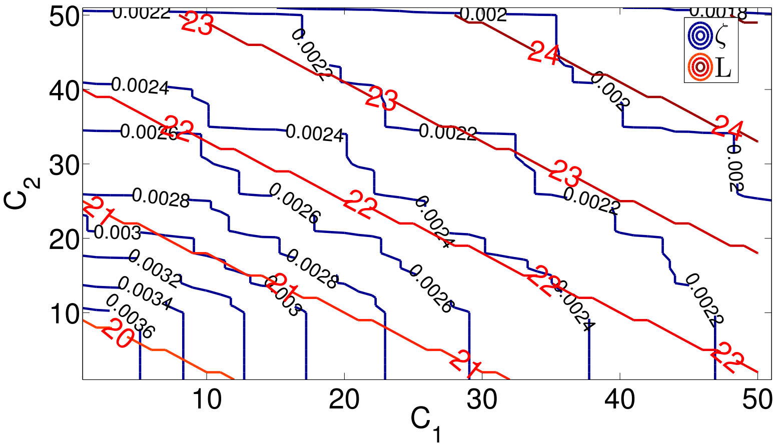

Figure 8: *Contour lines of relative error (blue) and of averaged L (red) in (C_1, C_2)-space.*

instead of $L_{\rm V}$ defined by (21). To further illustrate this choice, which is retained thereafter, Fig 7, shows $\xi(\beta)$ defined by (20) as a function of β for the uniform and Gaussian distributions of points and $(C_1, C_2) = (0, 0)$, $(50, 50)$ or $(60, 0)$. In particular, the combination $(C_1, C_2) = (60, 0)$ is seen to return an almost constant accuracy over the damping range of interest, while $(C_1, C_2) = (0, 0)$ leads to a deteriorating accuracy as β increases.

4 FULL ML-FMBEM EXAMPLES IN 3-D VISCO-ELASTODYNAMICS

In this section, the effect of introducing the complex wavenumbers $k^\star_{P,S}$ into the complete ML-FMBEM formulation, and in particular the importance of evaluating the kernels $G(r; k^\star_{P,S})$ using the damping-dependent selection rule (23) for L, are studied on two 3D visco-elastodynamic examples for which analytical solutions are known. Both examples involve a spherical cavity of radius R embedded in a viscoelastic isotropic infinite medium. In the first example the cavity surface is subjected to a time-harmonic uniform pressure P (Fig. 9.a), while the second example considers the scattering by the cavity, now assumed traction-free, of an incident plane P-wave (Fig. 9.b) defined by $\mathbf{u}_{\rm inc} = \boldsymbol{\nabla} \exp\bigl(ik^\star_P z - \beta k_P R\bigr)$. The corresponding analytic solutions are given for convenience in the Appendix. Only the surface of the spherical cavity is meshed. The Poisson ratio is set to $\nu = 0.25$, and the dimensionless frequency defined as $\eta_P = k_P R/\pi$. Three values of η_P have been considered, with the size of the models adjusted so as to maintain a mesh density of about 10 points per S-wavelength, see Table 1.

The results obtained by selecting L according to either the existing real-wavenumber rule $L_{\rm E}$ (18) or the proposed complex-wavenumber rule $L'(\cdot, \beta, C)$ (23) are compared, in terms of relative RMS error,

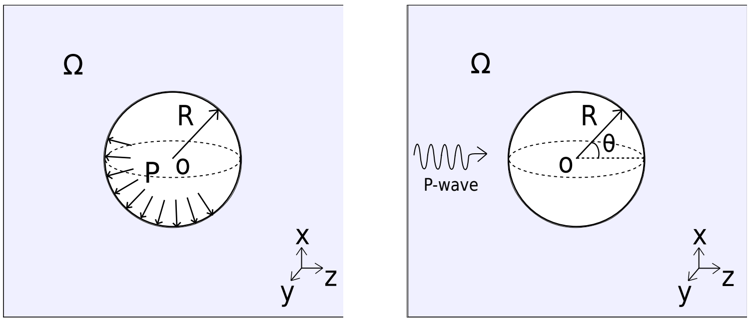

(a) (b)

Figure 9: *Geometry and notation: (a) pressurized spherical cavity, and (b) diffraction of a P-wave by a spherical cavity.*

Mesh	sphere3	sphere4	sphere5
N	7 686	30 726	122 886
η_P	1.5	3	6
Nb. levels	4	5	6

Table 1: *Reference tests for the cavity problems.* $\eta_P = k_P R/2\pi$ *is the normalized frequency.*

Level	L		
	$\eta_P = 1.5$	$\eta_P = 3.$	$\eta_P = 6.$
2	15	24	40
3	10	15	24
4	—	10	15
5	—	—	10

Level	L			
	$C = 0$	$C = 60$	$C = 120$	$C = 150$
2	24	31	38	42
3	15	21	27	30
4	10	15	20	22

Table 2: *Spherical cavity example: values of* L *at the active levels given by rule* (18) *for the results of Fig. 10 (left) and by rule* (23) *for the results of Fig. 11 (right)*

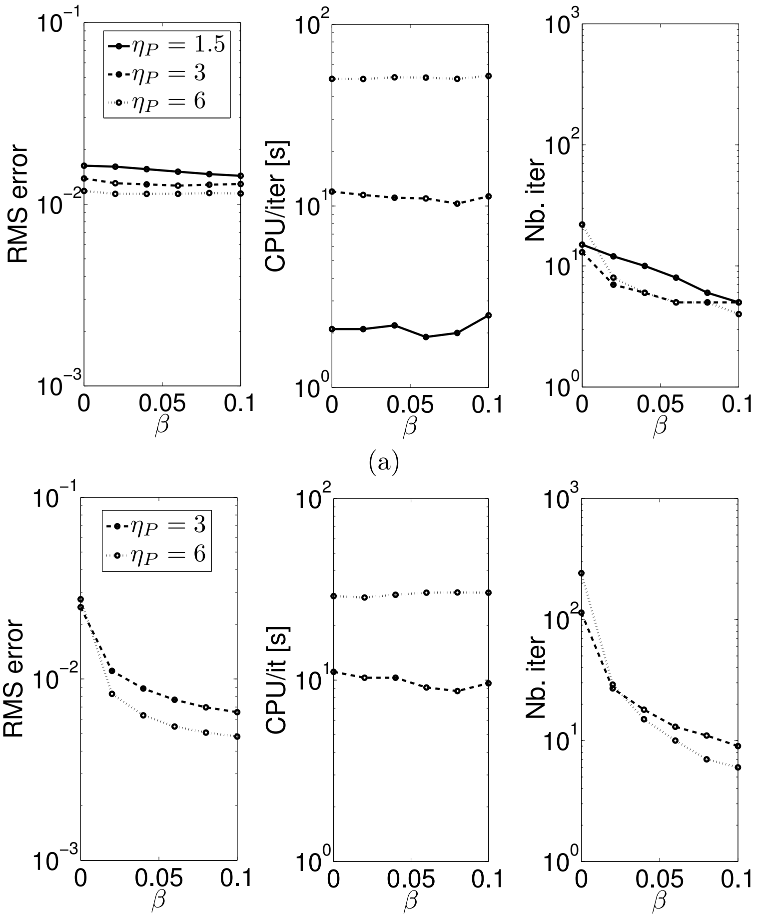

(a)

(b)

Figure 10: *Spherical cavity example: results obtained by selecting* L *using the real-wavenumber rule* L_E*, for (a) the pressurized spherical cavity, and (b) the scattering of a P-wave by a spherical cavity.*

CPU time per GMRES iteration and number of GMRES iterations, for the two examples considered. Moreover, the values of L at the active levels given by rules (18) and (23) are given in Table 2.

Performance of the previous rule $L_{\rm E}$. When $L_{\rm E}$ is used (Fig. 10), i.e. for L independent on β, the relative RMS error remains almost constant (or slightly decreases) as β increases, with the CPU time per iteration also relatively insensitive to β, and GMRES converges within fewer iterations. The reduction in the iteration count is ascribed to the exponential spatial decay of $G(r;k^\star)$ with r for $\beta > 0$, which balances the loss of accuracy in the kernel approximation.

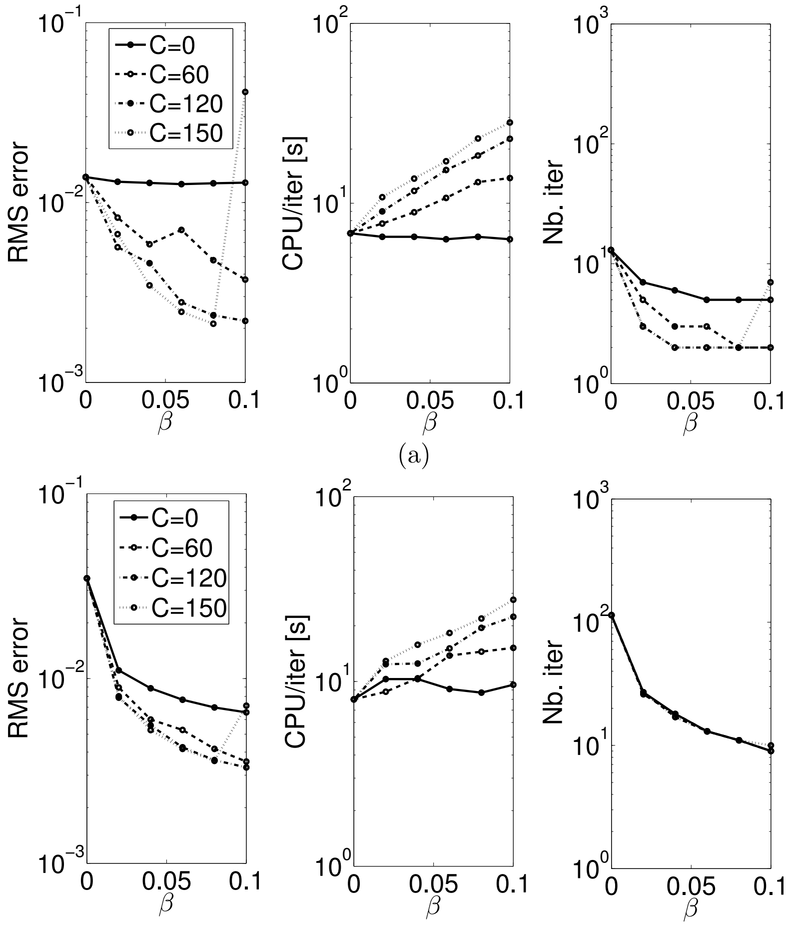

(a)

(b)

Figure 11: *Influence of different values of the constant C in relation* (23) *: pressurized cavity (a) and scattering by a spherical cavity (b) for $\eta_P = 3$.*

Performance of the new β-dependent rule $L'_{\rm V}$. To evaluate the influence of the constant C, the two examples have been solved using several different values of C in $L'_{\rm V}(\cdot,\beta,C)$; results are shown in Fig. 11. In addition to the improved accuracy in the evaluation of G permitted by rule (23) (see Sec. 3.2), this choice yields increasing solution accuracy (i.e. decreasing relative RMS solution error), at the cost of a growing CPU time (due to the $\mathcal{O}(L^2)$ quadrature points) as β increases. The case $C = 0$ corresponds to $L'_{\rm V} = L_{\rm E}$ (real-wavenumber rule) and is reported for comparison. When too-large L are generated ($C = 150$), the divergence threshold of the Hankel functions is reached for $\beta = 0.1$, with a sharp drop in solution accuracy. The choice $C = 60$, which yields an approximately constant accuracy in the evaluation of G, offers a good compromise in terms of computational efficiency. Hence, the final proposed damping-dependent selection rule is:

$$L''_{\rm V}(D;\beta) = k^\star D + (7.5 + 60\beta)\log_{10}(k^\star D + \pi) = L'_{\rm V}(D;\beta,60) \tag{24}$$

Results obtained on the two example configurations using the selection rule (24) are reported in Fig. 12. The good agreement between the ML-FMBEM and analytical solutions is also evident on

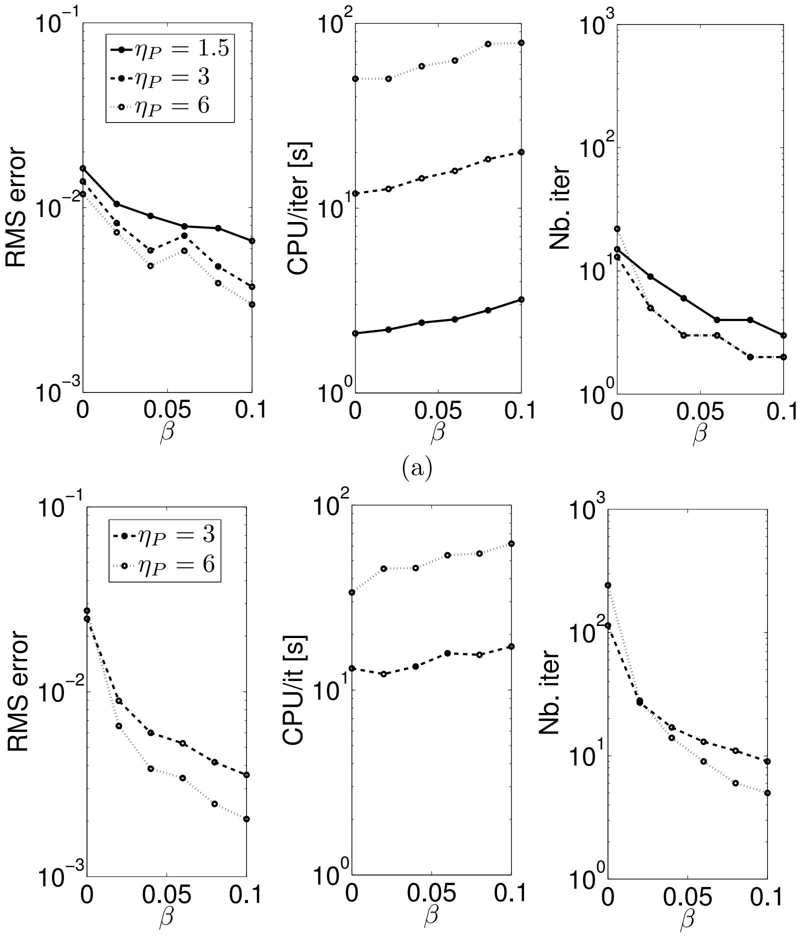

(a)

(b)

Figure 12: *Results using* $L = L''_V$*: pressurized cavity (a) and scattering by a spherical cavity (b)*

Fig. 13 for the scattering problem, with comparisons for the total radial displacement along radial lines emanating from the sphere shown for several azimuths ($\theta = 0$, $\pi/4$, $\pi/2$, $3\pi/4$, π) and damping factors ($\beta = 0$, 0.04, 0.08). For $0 \leq \theta \leq \pi/2$, the amplitude reduction occurring with increasing damping is clearly seen. For $\theta > \pi/2$, the amplitude growth with β is due to the apparent backward propagation on the r/R axis (forward amplitude decay appearing as a backward exponential growth).

Remarks on the cell size threshold. The possibility to adjust the cell size threshold $d_{min} = \alpha\lambda_S$ (Sec. 2) as a function of β is now investigated. Recall that $\alpha = 0.3$ was found to be suitable in the elastodynamic case [26]. Setting $\alpha = 0.15$ instead adds one level to the octree. This extra level results in loss of solution accuracy (of about one order of magnitude in terms of RMS), which for viscoelastic cases is only partially compensated by the accuracy gains observed for increasing β, see Fig. 14 where the effect of an extra level is tested for the two examples, with L set using (24). In Fig. 14b, the relative RMS error for $\alpha = 0.15$ and $\beta > 0.08$ has a value comparable to the elastodynamic combination $\alpha = 0.3$ and $\beta = 0$ (in which case adding the new level led to acceptable results). However, this is not the case for the other example. Thus, the presence of viscoelastic damping does not appear to allow a modification of $\alpha = 0.3$, e.g. by making it dependent upon β, that is guaranteed to yield uniform acceptable solution accuracy. In fact, a simple β-dependent rule for determining $\alpha = 0.3$ was tried, leading to similar conclusions.

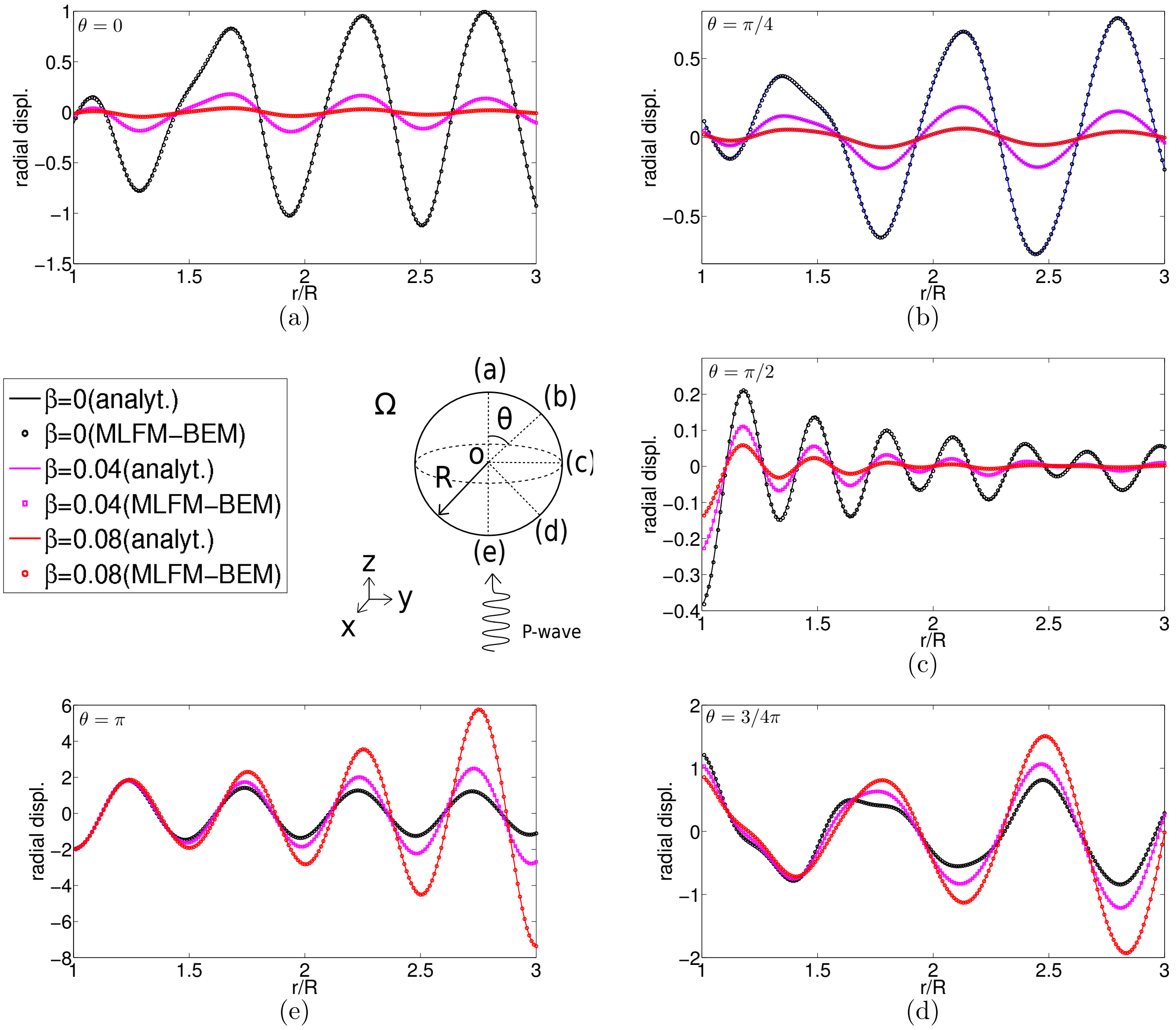

Figure 13: *Scattering of an incident plane P-wave by a spherical cavity (with $\eta_P = 4$): comparison between the ML-FMBEM and analytical solutions (radial displacement along radial lines emanating from the sphere) for several azimuths ($\theta = 0,\ \pi/4,\ \pi/2,\ 3\pi/4,\ \pi$) and damping factors ($\beta = 0,\ 0.04,\ 0.08$).*

5 MULTI-DOMAIN ML-FMBEM IN 3-D VISCO-ELASTODYNAMICS

5.1 The multi-domain BE-BE coupling

Wave propagation analyses often involve heterogeneous media (e.g. seismic waves in geological structures). Following the single-domain elastodynamic ML-FMBEM formulation [26], allowing to study e.g. the amplification by topographical irregularities of seismic waves propagating in homogeneous media, a multi-region version of the elastodynamic ML-FMBEM was proposed in [17]. Therein the elastic propagation medium is partitioned into n piecewise-homogeneous subdomains Ω_i ($1 \le i \le n$, $\Omega = \cup_i \Omega_i$). For each Ω_i, a separate octree structure is defined, a boundary integral equation is formulated and the corresponding contributions to the global matrix-vector product are computed. To ensure a global square system of equations, linear combinations of the BE equations arising from collocation at nodes or interfacial element shared by more than one subregion are defined, and the global matrix-vector product is evaluated by combining accordingly the contributions coming from the various interfaces relative to each subregion. Details on this elastodynamic ML-FM-based BE-BE coupling strategy are given in [17].

The possibility to account for material damping allows a more realistic modelling of seismic wave propagation in alluvial soil deposits, which are lossy materials. Here, the previously discussed alterations

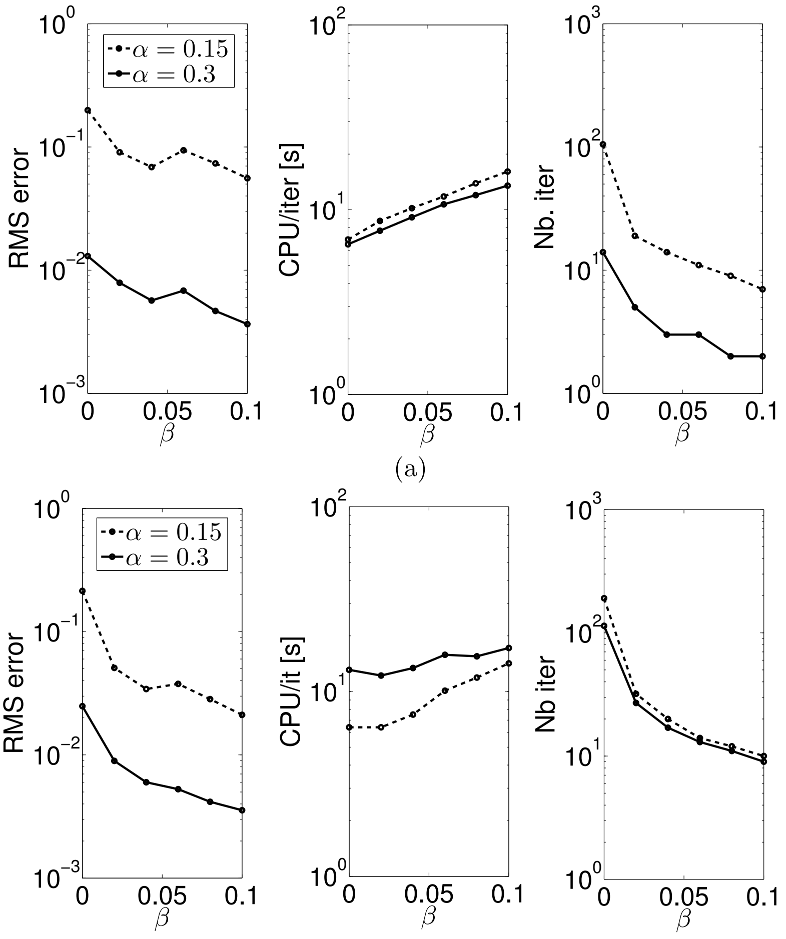

(a)

(b)

Figure 14: *Influence of the cell size threshold $\alpha = 0.3, 0.15$ using the proposed $L-$relation: pressurized cavity (a) and scattering by a spherical cavity (b).*

to the previous elastodynamic ML-FMBEM allowing its extension to visco-elastodynamics have been introduced into the multi-domain ML-FM BE-BE. The visco-elastodynamic multi-domain ML-FM BE-BE thus obtained is now studied on numerical examples derived from those of [17], in order to study the effect of damping.

5.2 Verification on a two-region example

Consider a spherical cavity of radius R_1, surrounded by a spherical layer Ω_1 of outer radius R_2 and embedded in a 3-D visco-elastic isotropic infinite medium Ω_2, submitted to an internal uniform time-harmonic pressure P, see Fig. 15. The materials in Ω_1 and Ω_2 are homogeneous and their mechanical properties are detailed in Table 3. This problem has an analytical solution, given in the Appendix.

The damping in Ω_2 is $\beta_2 = 0.05$, while various values in the range $0 \leq \beta_1 \leq 0.1$ are considered for Ω_1. The size of the problem is $N = 307,224$, and the octree for each region has a leaf level $\bar{\ell}_1 = \bar{\ell}_2 = 5$. This problem has been solved with L set using either the elastic rule (18) or the damping-dependent rule (24). Results on the relative error between the numerical and analytical solutions for the displacement on the cavity wall and the interface between Ω_1 and Ω_2 are shown in Fig. 16, while the values of L_1 at the active levels $\ell_1 = 2, 3, 4$ given by rules (18) and (24) are reported in Table 3. Compared to the elastic rule L_{E}, the proposed damping-dependent rule L''_{V} brings improvement on solution accuracy while requiring fewer GMRES iterations, each iteration being however somewhat more expensive due to the fact that $L''(D; \beta)$ increases with β.

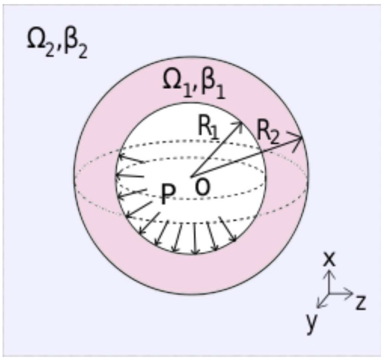

Figure 15: *Multi-domain validation problem.*

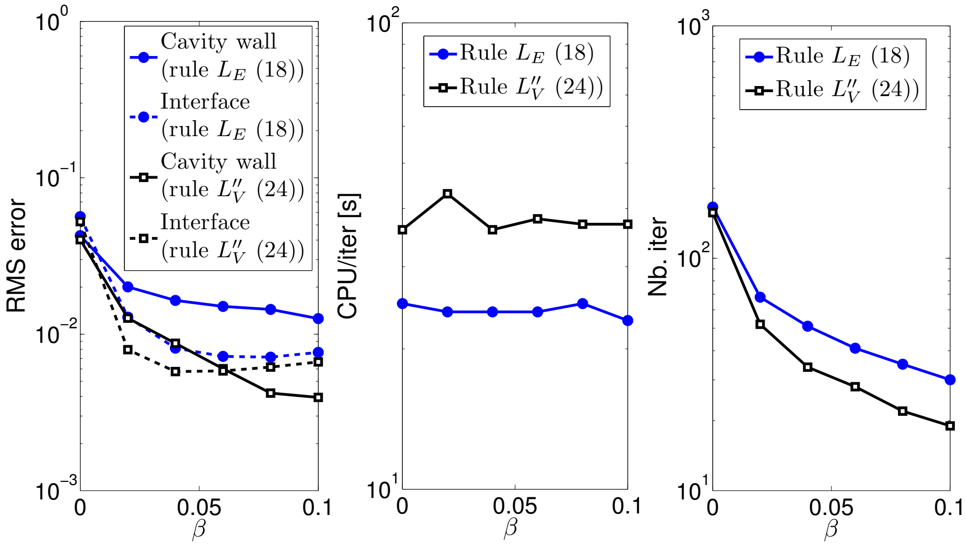

Figure 16: *Two-region example, comparison of results obtained with L set using either L_E (18) or L''_V (24).*

(a) (b)

Figure 17: *Vertically incident P-wave in a viscoelastic half-space containing a semi-spherical soft basin: geometry and finite boundary element discretization.*

5.3 Seismic wave propagation in a canonical damped basin

In this section, an example previously used in [49] and [17] for elastic waves is considered, where a vertically-incident plane P-wave propagates in a viscoelastic half-space containing a semi-spherical soft basin Ω_2 (Fig. 17). As the present FM-BEM is based on the full-space fundamental solution, the BE

	μ	ν	ρ
Ω_1	4	0.25	3
Ω_2	2	1/3	1

ℓ	$L_1^{(\ell)} = L_{\mathrm{E}}(\cdot)$	$L_1^{(\ell)} = L''_{\mathrm{V}}(\cdot;\beta_1)$	
		$(\beta_1 = 0.04)$	$(\beta_1 = 0.1)$
2	25	28	32
3	16	18	22
4	10	13	15

Table 3: *Two-region example: material properties (left), value of L_1 for active levels 2, 3, 4 using rules* (18) *or* (24), *for $\beta_1 = 0.04$ or 0.1 (right).*

$k_P^{(1)}R/\pi$	N	d_{min}/λ_S	$\bar{\ell}_1$; $\bar{\ell}_2$	CPU/Iter;Nb Iter ($\beta = 0$)	CPU/Iter ;Nb Iter ($\beta = 0.05$)	CPU/Iter;Nb Iter ($\beta = 0.1$)
0.5	17,502	0.15	5; 4	7.6; 26	7.7; 23	9.2; 22
0.7	17,502	0.15	6; 4	5.7; 34	5.9; 27	7.1; 24
1	90,057	0.3	5; 4	62.6; 51	72.7; 34	95.5; 29
2	190,299	0.3	6; 5	120.3; 95	153.7; 49	189.9; 35

Table 4: *Vertically incident P-wave in a viscoelastic half-space containing a semi-spherical soft basin: computational data and results.*

mesh must include the free surface (Fig. 17, here truncated within a radius $D = 5R$ centered at the basin center). The basin Ω_2 and the complementary semi-infinite medium Ω_1 are constituted of homogeneous, isotropic and visco-elastic materials, with equal damping ratios ($\beta^{(1)} = \beta^{(2)} = \beta$) and other mechanical parameters such that $\nu^{(1)} = 0.25$, $\nu^{(2)} = 1/3$, $\mu^{(2)} = 0.3\mu^{(1)}$ and $\rho^{(2)} = 1.2\rho^{(1)}$. Four different normalized frequencies $\eta_P = k_P^{(1)}R/\pi$ are considered. Computational data and results are summarized, for each frequency and damping values $\beta = 0.0$, 0.05, 0.1, in Table 4, in terms of BEM model size N, cell division threshold $\alpha = d_{\min}/\lambda_S$, number of levels of the octree for each subregion, CPU time per GMRES iteration, and GMRES iteration count. The results obtained are consistent with observations made in the previous sections. In particular, for increasing β, the iteration count drops while the CPU time per iteration increases. Moreover, the necessary coincidence of the results for $\beta = 0$ with the corresponding ones of [17] has been successfully checked.

Contour maps for the vertical and horizontal displacements, u_z and u_y, on the free surface are shown in Fig. 18 for three levels of damping β, illustrating the effect of damping on the basin response. The surface displacements are then compared in Fig. 19 with corresponding (elastic) results reported in [17] for the four frequencies $\eta_P = 0.5$, 0.7, 1.0, 2.0. Damping is seen to reduce by up to roughly 30% (case $k_P^{(1)}R/\pi = 0.5$, $\beta = 0.1$) the magnitude of the vertical displacement at the basin center, compared to the undamped case.

Influence of the truncation radius D. An interesting issue concerns the choice of the truncation radius D of the discretized free surface, i.e. the smallest value $D_{\min}$ of D for which the solution is insensitive to the free-surface truncation. Such parametric studies were conducted for the elastic case in [17], and the results compared with those obtained using a semi-analytical approach in [49]. Here, it is important to determine how $D_{\min}$ depends on damping. Figure 20a shows $|u_z|$ on the soft basin surface computed using meshes corresponding to different values D. The oscillations reflecting the sensitivity of the solution to the choice of D in the elastic case ($\beta = 0$) are apparent. Convergence was found to be achieved for $D \geq 13R$ in the elastic case [17], with oscillations of up to ±4% about the reference solutions when using $D < 13R$. Here, with $\beta = 0.05$, such oscillations are strongly reduced, as shown in Fig. 20b. Figure 21 emphasizes these observations by plotting the ratio $|u_z|(D)/|u_z|_{\mathrm{ref}}$ at the basin center, with $|u_z|(D)$ computed using given truncation radius D and $|u_z|_{\mathrm{ref}} := |u_z|(D = 20R)$ a reference solution obtained using $D = 20R$, the normalized frequency being set to $\eta_P = 0.5$. The fact that damping reduces the solution errors caused by the free surface truncation allows to use lower values of D when dealing with viscoelastic media, with truncation values $D_{\min} = 6R$ (resp. $D_{\min} = 3R$) found to be suitable for $\beta = 0.05$ (resp. $\beta = 0.1$).

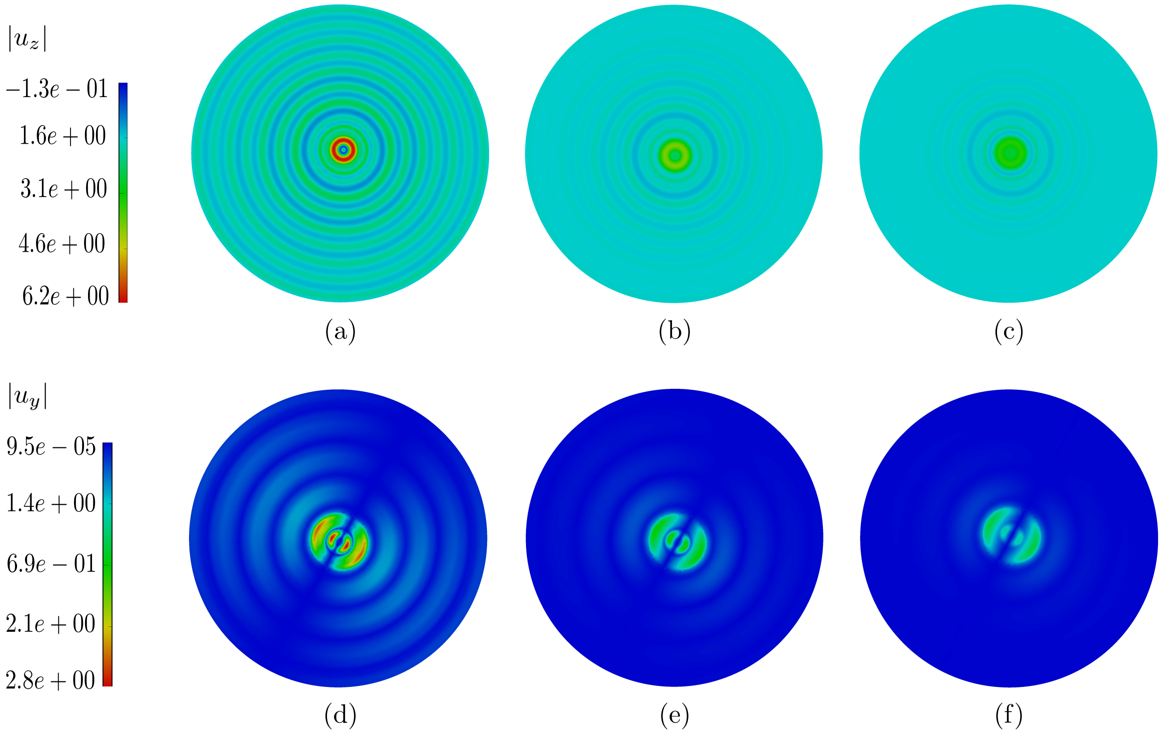

(a) (b) (c)

(d) (e) (f)

Figure 18: *Vertically incident P-wave in a viscoelastic half-space containing a semi-spherical soft basin: contour maps of* $|u_z|$ *(a,b,c) and* $|u_y|$ *(d,e,f) at* $k_P^{(1)}R/\pi = 2$ *for three levels of damping in both media* ($\beta_1 = \beta_2 = \beta$)*: (a,d)* $\beta = 0$ *(purely elastic case), (b,e)* $\beta = 0.05$ *and (c,f)* $\beta = 0.1$.

5.4 Some remarks on preconditioning

This article does not address the very important, and still largely open, issue of preconditioning the FMBEM. Frequently-used techniques include block-diagonal preconditioners [50, 51], the incomplete LU factorization with threshold [52], the flexible generalized minimal residual method (fGMRES) proposed in [53] and used e.g. in [54] for the 3-D Helmholtz equation), the sparse approximate inverse (SPAI [55]). More recently, a preconditioning based on the Calderon identities for periodic transmission problems for the 3-D Helmholtz equation has been proposed [56] for accelerating the convergence in the presence of sharp solution variations caused by high velocity contrasts.

For multi-domain problems, the system matrix is populated with various blocks whose magnitude depend on material properties, with magnitude disparities leading to significant increases in GMRES iteration count. In a previous work [17], an equation scaling approach was implemented and shown on various examples to reduce this problem. The iteration count is nevertheless known to increase with N or k. A simple preconditioning strategy is proposed in [57], where the matrix of near interactions (i.e. gathering the contributions from adjacent cells to the influence matrix $\mathbb{K}$) is used in a preconditioning matrix equation, which is solved using GMRES set with a low accuracy threshold (hence the iterative solution algorithm features two nested GMRES solvers).

No preconditioner was used in this work, in order to compare "raw" versions of the FMBEM with or without attenuation. The latter, moreover, does not appear to harm the GMRES convergence, since the iteration count was usually found to reduce as β increases (see Figs. 10-12). The inner-outer preconditioned GMRES solver previously used for the elastodynamic FMBEM can easily, and in due course will, be incorporated into the present visco-elastodynamic FMBEM, with expected computational savings similar to those observed in [57].

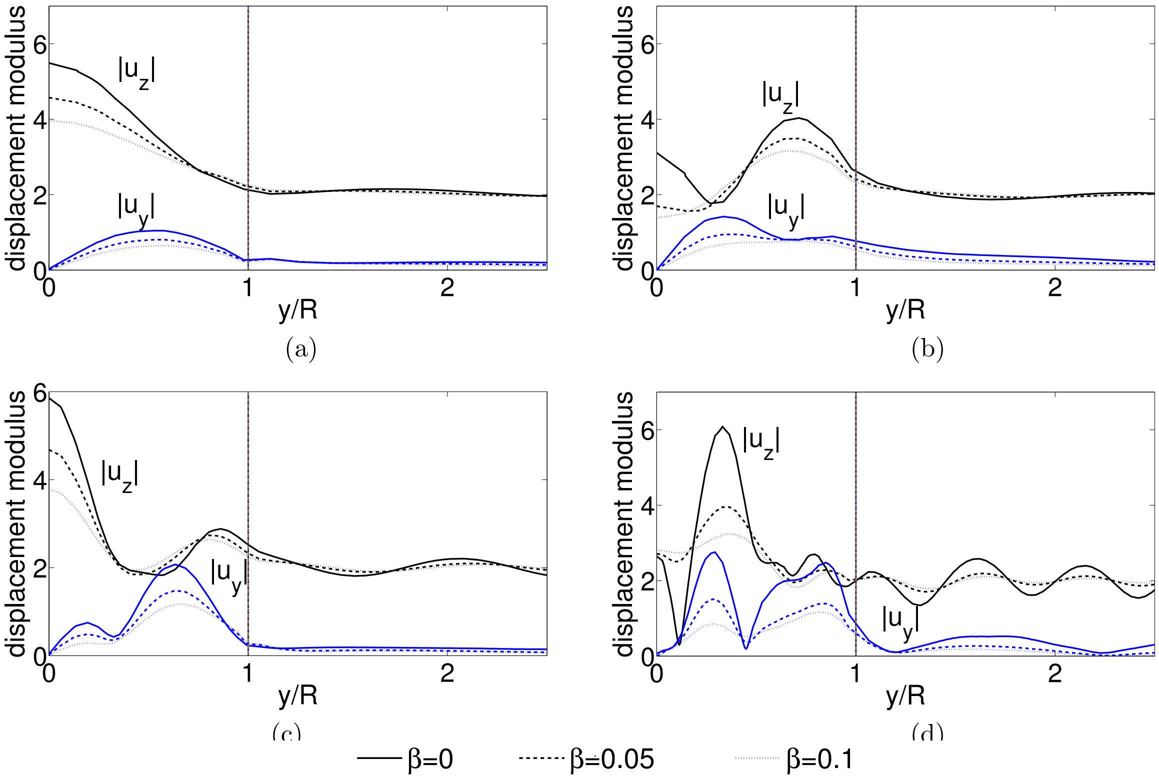

(a) (b) (c) (d)

Figure 19: *Vertically incident P-wave in a viscoelastic half-space containing a semi-spherical soft basin: influence of the damping* ($\beta = 0,\ 0.05,\ 0.1$) *on the surface displacements* $|u_y|$ *and* $|u_z|$ *at* $k_P^{(1)}R/\pi = 0.5$ *(a),* 0.7 *(b),* 1 *(c) and* 2 *(d).*

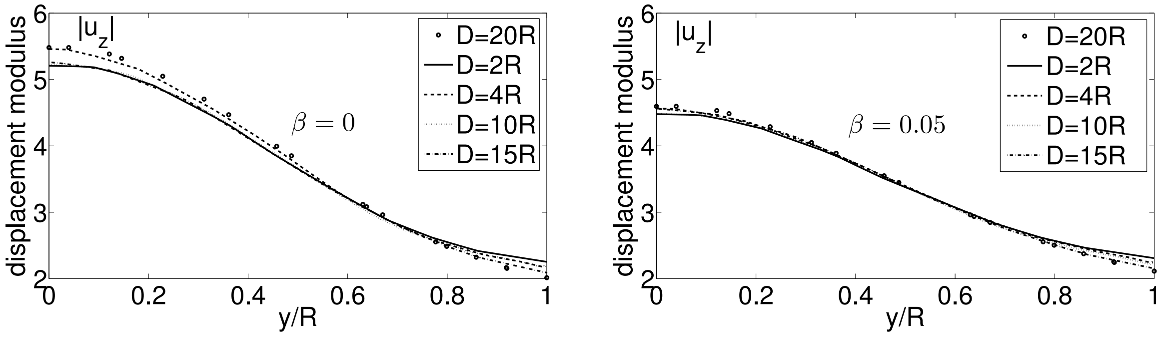

(a) (b)

Figure 20: *Vertically incident P-wave in a viscoelastic half-space containing a semi-spherical soft basin: influence of damping on the basin surface displacements at* $k_P^{(1)}R/\pi = 0.5$ *for different free surface truncation radii* $D/R = 2,\ 4,\ 10,\ 15,\ 20$*: (a)* $\beta = 0$*, i.e. elastic case; (b)* $\beta = 0.05$.

6 CONCLUSIONS

In this paper, the application of a previously-published ML-FMBEM for 3-D time-harmonic elastodynamics (involving real wavenumbers) to linear visco-elastodynamics (involving complex wavenumbers, with a small imaginary part accounting for weakly dissipative materials) has been investigated. While the underlying BIE and FM formulations are formally identical to that of elastodynamics, the presence

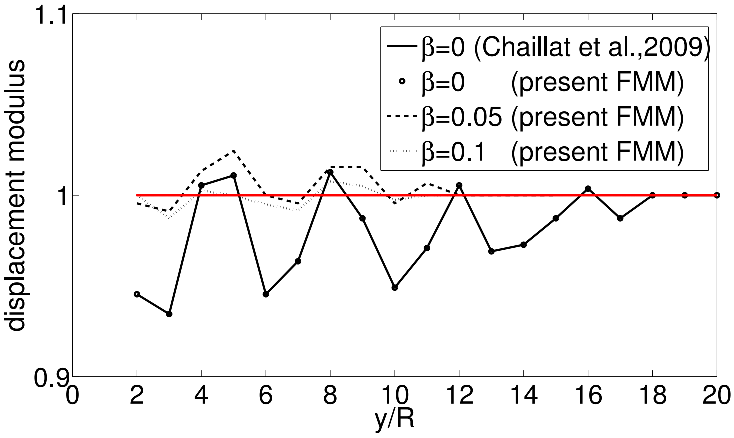

Figure 21: *Vertically incident P-wave in a viscoelastic half-space containing a semi-spherical soft basin: ratio $|u_z|(D)/|u_z|_{\text{ref}}$ for the vertical displacement at the basin center, with $|u_z|_{\text{ref}} := |u_z|(D=20R)$.*

of complex wavenumbers called for a reassessment of the main settings of the ML-FMBEM, and especially of the level-dependent rule for choosing the truncation parameter L. An empirical study has been conducted, showing that a modified, damping-dependent selection rule for L improves the average accuracy for the evaluation of the visco-elastodynamic fundamental solution over a range of material damping ratio values β consistent with intended applications in civil engineering or geophysics. The resulting visco-elastodynamic ML-FMBEM has been tested on several 3D example problems involving either single-domain or multi-domain configurations, with comparisons to known analytical solutions made in both cases. These examples involved BE models of size up to $N \approx 3\,10^5$ boundary unknowns. Finally, the multi-region formulation was applied to the problem of a (seismic) wave propagating in a semi-infinite medium with a lossy semi-spherical inclusion (seismic wave in alluvial basin). The influence of the truncation radius on the free surface was tested on this problem, using BE models of size up to $N \approx 2\,10^5$. As expected, accounting for material damping was found to permit lower values of the truncation spatial radius than in the purely elastic case, implying substantial savings on the BE model size.

A ANALYTICAL SOLUTIONS FOR TEST PROBLEMS

A.1 Spherical cavity under uniform pressure

Let R be the radius of a spherical cavity embedded in a viscoelastic isotropic infinite medium and subjected to an internal time-harmonic uniform pressure P. This spherically-symmetric problem has a closed-form solution, with the radial displacement and stress given (with $\alpha = \mathrm{i}k_P^{\star}R$, $\theta = 4(1-\alpha)+\alpha^2/\gamma^{\star 2}$ and $\gamma^{\star}$ defined as in (8)), by

$$u_r(r) = \frac{PR^2}{\mu^{\star}\theta r^2}(R-\alpha r)\exp\Big[\alpha\Big(\frac{r}{R}-1\Big)\Big], \qquad \sigma_{rr}(r) = \frac{PR}{\theta r^3}\Big(-\frac{\alpha r}{\gamma^{\star 2}}+4\alpha Rr-4R^2\Big)\exp\Big[\alpha\Big(\frac{r}{R}-1\Big)\Big] \quad (25)$$

A.2 Spherical cavity under uniform pressure surrounded by a spherical shell

This spherically-symmetric problem also has a closed-form solution. Referring to Fig. 15, the radial displacement $u_r^{(i)}$ in domains Ω_i $(i=1,2)$ is such that $u_r^{(i)} = \partial\phi_i/\partial r$, with potentials ϕ_i given by

$$\phi_1 = \frac{A_1}{r}\exp(\mathrm{i}k_P^{\star(1)}r) + \frac{B_1}{r}\exp(-\mathrm{i}k_P^{\star(1)}r), \qquad \phi_{=}\frac{A_2}{r}\exp(\mathrm{i}k_P^{\star(2)}r) \quad (26)$$

where the coefficients A_1, A_2, B_1 are found by solving

$$\begin{bmatrix} e^{\alpha_1}(\alpha_1-1) & -e^{-\alpha_1}(\alpha_1+1) & e^{\alpha_2}(1-\alpha_2) \\ e^{\alpha_1}\mu_1\theta_1 & e^{-\alpha_1}\mu_1(\theta_1+8\alpha_1) & -e^{\alpha_2}\mu_2\theta_2 \\ e^{\alpha_3}\mu_1\theta_3 & e^{-\alpha_3}\mu_1(\theta_3+8\alpha_3) & 0 \end{bmatrix} \begin{Bmatrix} A_1 \\ B_1 \\ A_2 \end{Bmatrix} = \begin{Bmatrix} 0 \\ 0 \\ -PR_1^3\gamma_1^{\star 2} \end{Bmatrix}$$

with $\alpha_1 = \mathrm{i}k_P^{\star(1)}R_2$, $\alpha_2 = \mathrm{i}k_P^{\star(2)}R_2$, $\alpha_3 = \mathrm{i}k_P^{\star(1)}R_1$ and $\theta_i = 4(1-\alpha_i) + \alpha_i^2/\gamma_i^{\star 2}$ $(i = 1, 2)$ where $\gamma_i^\star$ is defined in each domain as in (25).

A.3 Scattering of a P-wave by a spherical cavity

$$u_r = \frac{1}{r}\sum_{n=0}^{+\infty}[\Phi_0 i^n(2n+1)U_1^{(1)}(k_P^\star r) + A_n U_1^{(3)}(k_P^\star r) + C_n U_3^{(3)}(k_S^\star r)]P_n(\cos\theta) \tag{27}$$

$$u_\theta = \frac{1}{r}\sum_{n=0}^{+\infty}[\Phi_0 i^n(2n+1)V_1^{(1)}(k_P^\star r) + A_n V_1^{(3)}(k_P^\star r) + C_n V_3^{(3)}(k_S^\star r)]\frac{\mathrm{d}}{\mathrm{d}\theta}P_n(\cos\theta) \tag{28}$$

with

$$\begin{aligned}
U_1^{(1)}(z) &= n j_n(z) - z j_{n+1}(z) & V_1^{(1)}(z) &= j_n(z)\\
U_1^{(3)}(z) &= n h_n^{(1)}(z) - z h_{n+1}^{(1)}(z) & V_1^{(3)}(z) &= h_n^{(1)}(z)\\
U_3^{(3)}(z) &= n(n+1)h_n^{(1)}(z) & V_3^{(3)}(z) &= (n+1)h_n^{(1)}(z) - z h_{n+1}^{(1)}(z)
\end{aligned}$$

and where the constants A_n, C_n, obtained from enforcing the traction-free boundary condition on the surface of the spherical cavity, are given by

$$\begin{aligned}
A_n &= \phi_0 i^n(2n+1)\left[T_{11}^{(1)}(k_P^\star R)\ \ T_{43}^{(3)}(k_S^\star R) - T_{41}^{(1)}(k_P^\star R)\ \ T_{13}^{(3)}(k_S^\star R)\right]/\Delta_n\\
C_n &= \phi_0 i^n(2n+1)\left[T_{11}^{(1)}(k_P^\star R)\ \ T_{41}^{(3)}(k_S^\star R) - T_{41}^{(1)}(k_P^\star R)\ \ T_{11}^{(3)}(k_S^\star R)\right]/\Delta_n
\end{aligned}$$

with

$$\begin{aligned}
T_{11}^{(1)}(z) &= (n^2 - n - \frac{1}{2}k_S^{\star 2}r^2)j_n(z) + 2z j_{n+1}(z)\\
T_{41}^{(1)}(z) &= (n-1)j_n(z) - z j_{n+1}(z)\\
T_{11}^{(3)}(z) &= (n^2 - n - \frac{1}{2}k_S^{\star 2}r^2)h_n^{(1)}(z) + 2z h_{n+1}^{(1)}(z)\\
T_{13}^{(3)}(z) &= n(n+1)[(n-1)h_n^{(1)}(z) - z h_{n+1}^{(1)}(z)]\\
T_{41}^{(3)}(z) &= (n-1)h_n^{(1)}(z) - z h_{n+1}^{(1)}(z)\\
T_{43}^{(3)}(z) &= (n^2 - 1 - \frac{1}{2}k_S^{\star 2}r^2)h_n^{(1)}(z) + z h_{n+1}^{(1)}(z)
\end{aligned}$$

and

$$\Delta_n = T_{11}^{(3)}(k_P^\star R)\ \ T_{43}^{(3)}(k_S^\star R) - T_{41}^{(3)}(k_P^\star R)\ \ T_{13}^{(3)}(k_S^\star R)$$

References

[1] Virieux J. P-SV wave propagation in heterogeneous media: velocity-stress finite-difference method. Geophysics 1986;51:889–901.

[2] Bohlen T. Parallel 3-D viscoelastic finite difference seismic modelling. Computers & Geosciences 2002;28:887–899.

[3] Bao H., Bielak J., Ghattas O., Kallivokas F., O'Hallaron D., Shewchuk J., Xu J. Large-scale simulation of elastic wave propagation in heterogeneous media on parallel computers. Computer Methods in Applied Mechanics and Engineering 1998;152:85–102.

[4] Semblat J., Brioist J. Efficiency of higher order finite elements for the analysis of seismic wave propagation. Journal Of Sound And Vibrations 2000;231:460–467.

[5] Faccioli E., Maggio F., Paolucci R., Quarteroni A. 2D and 3D elastic wave propagation by a pseudo-spectral domain decomposition method. Journal of Seismology 1997;1:237–251.

[6] Komatitsch D., Vilotte J. The spectral element method: an efficient tool to simulate the seismic response of 2D ans 3D geological structures. Bulletin of the Seismological Society of America 1998; 88:368–392.

[7] Clayton R., Engquist B. Absorbing boundary conditions for acoustic and elastic wave equations. Bulletin of the Seismological Society of America 1977;67:1529–1540.

[8] Mur G. Absorbing boundary conditions for the finite-difference approximation of the time-domain electromagnetic-field equations. IEEE Transactions on Electromagnetic Compatibility 1981;EMC-23:377 –382.

[9] Festa G., Nielsen S. PML absorbing boundaries. Bulletin of the Seismological Society of America 2003;93:891–903.

[10] Semblat J., Lenti L., Gandomzadeh A. A simple multi-directional absorbing layer method to simulate elastic wave propagation in unbounded domains. International Journal for Numerical Methods in Engineering 2011;85:1543–1563.

[11] Bécache E., Fauqueux S., Joly P. Stability of perfectly matched layers, group velocities and anisotropic waves. Journal of Computational Physics 2003;188:399–433.

[12] Bettess P. Infinite elements. Penshaw Press, 1992.

[13] Brebbia C.A., Telles J.C.F., Wrobel L.C. Boundary element techniques. Springer, 1984.

[14] Bonnet M. Boundary Integral Equation Methods for Solids and Fluids. Wiley, 1999.

[15] Rokhlin V. Diagonal forms of translation operators for the Helmholtz equation. Appl. Computat. Harmon. Analysis 1993;1:82–93.

[16] Bapat M.S., Shen L., Liu Y.J. Adaptive fast multipole boundary element method for three-dimensional half-space acoustic wave problems. Engineering Analysis with Boundary Elements 2009; 33:1113–1123.

[17] Chaillat S., Bonnet M., Semblat J. A new fast multi-domain BEM to model seismic wave propagation and amplification in 3D geological structures. Geophysical Journal International 2009;177:509–531.

[18] Frangi A., Di Gioia A. Multipole BEM for the evaluation of damping forces on MEMS. Computational Mechanics 2005;37:24–31.

[19] Chew W., Chao H., Cui T., Ohnuki S., Pan Y., Song J., Velamparambil S., Zhao J. Fast integral equation solvers in computational electromagnetics of complex structures. Engineering Analysis with Boundary Elements 2003;27:803–823.

[20] Börm S., Grasedyck L., Hackbusch W. Introduction to hierarchical matrices with applications. Engineering Analysis with Boundary Elements 2003;27:405–422.

[21] Kurz S., Rain O., Rjasanow S. The adaptive cross approximation technique for the 3D boundary element method. IEEE Transactions on Magnetics 2002;38:421–424.

[22] Messner M., Schanz M. An accelerated symmetric time-domain boundary element formulation for elasticity. Engineering Analysis with Boundary Elements 2010;34:944–955.

[23] Nishimura N. Fast multipole accelerated boundary integral equation methods. Applied Mechanics Reviews 2002;55:299–324.

[24] Gumerov N.A., Duraiswami R. Fast multipole methods for the Helmholtz equation in three dimensions. Elsevier, 2005.

[25] Darve E. The fast multipole method I: error analysis and asymptotic complexity. SIAM Journal of Numerical Analysis 2000;38:98–128.

[26] Chaillat S., Bonnet M., Semblat J.F. A multi-level fast multipole BEM for 3-D elastodynamics in the frequency domain. Computer Methods in Applied Mechanics and Engineering 2008;197:4233–4249.

[27] Geng N., Sullivan A., Carin L. Multilevel fast-multipole algorithm for scattering from conducting targets above or embedded in a lossy half space. IEEE Transactions on Geoscience and Remote Sensing 2000;38:1561–1573.

[28] Geng N., Sullivan A., Carin L. Fast multipole method for scattering from an arbitrary PEC target above or buried in a lossy half space. IEEE Transactions on Antennas and Propagation 2001;49:740–748.

[29] Frangi A., Bonnet M. On the application of the Fast Multipole Method to Helmholtz-like problems with complex wavenumber. Computer Modeling in Engineering and Sciences 2010;58:271–296.

[30] Yasuda Y., Sakuma T. Analysis of sound fields in porous materials using the fast multipole BEM. In *37th International Congress and Exposition on Noise Control Engineering, Shangai, China*, 2008, 2008; .

[31] Gaul L. The influence of damping on waves and vibrations. Mechanical Systems and Signal Processing 1999;13:1–30.

[32] Christensen R. Theory of viscoelasticity. Dover, 1982.

[33] Dominguez J. Boundary elements in dynamics. Computational Mechanics Publications, Southampton Boston, 1993.

[34] Bourbié T., Coussy O., Zinszner B. Acoustics of porous media. Technip, 1987.

[35] Delépine N., Lenti L., Bonnet G., Semblat J.F. Nonlinear viscoelstic wave propagation: an extension of nearly constant attenuation models. ASCE J. Eng. Mech. 2009;135:1305–1314.

[36] Semblat J., Pecker A. Waves and vibrations in soils: earthquakes, traffic, shocks, construction works. IUSS Press, 2009.

[37] Lai C., Rix G. Simultaneous inversion of Rayleigh phase velocity and attenuation for near-surface site characterization. Tech. rep., National Science Foundation and U.S. Geological Survey, Georgia Institute of Technology, 1998.

[38] Kramer S. Geotechnical earthquake engineering. Prentice-Hall International Series in Civil Engineering and Engineering Mechanics, 1996.

[39] Eringen A.C., Suhubi. E.S. Elastodynamics, Vol. II-linear theory. Academic Pres, 1975.

[40] Saad Y. Iterative methods for sparse linear systems. SIAM, second edn., 2003.

[41] Rahola J. Diagonal forms of the translation operators in the fast multipole algorithm for scattering problems. BIT Numerical Mathematics 1996;36:333–358.

[42] Darve E. The fast multipole method: numerical implementation. Journal of Computational Physics 2000;160:195–240.

[43] Abramowitz M., Stegun I. Handbook of Mathematical Functions. Dover, 1964.

[44] Coifman R., Rokhlin V., Wandzura S. The Fast Multipole Method for the wave equation: a pedestrian description. IEEE Antennas and Propagation Magazine 1993;35:7–12.

[45] Koc S., Song J., Chew W. Error analysis for the numerical evaluation of the diagonal forms of the scalar spherical addition theorem. SIAM Journal on Numerical Analysis 1999;36:906–921.

[46] Song J., Chew W. Error analysis for the truncation of multipole expansion of vector green's functions. IEEE Microwave and Wireless Components Letters 2001;11:311–313.

[47] Du Toit C. The numerical computation of bessel functions of the first and second kind for integer orders and complex arguments. IEEE Transactions on Antennas and Propagation 1990;38:1341–1349.

[48] Heckmann D., Dvorak S. Numerical computation of Hankel functions of integer order for complex-valued arguments. Radio Science 2001;36:1265–1270.

[49] Sanchez-Sesma F. Diffraction of elastic waves by three-dimensional surface irregularities. Bulletin of the Seismological Society of America 1983;73:1621–1636.

[50] Fujiwara H. The fast multipole method for solving integral equations ofthree-dimensional topography and basin problems. Geophysical Journal International 2000;140(1):198–210.

[51] Song J., Cai-Cheng L., Chew W. Multilevel Fast Multipole Algorithm for Electromagnetic Scattering by Large Complex Objects. IEEE Transactions On Antennas And Propagation 1997;45(10):1488–1493.

[52] Sertel K., Volakis John L. Incomplete LU Preconditioner for FMM Implementation. Microwave And Optical Technology Letters 2000;26(4):265–267.

[53] Saad Y. A flexible inner-outer preconditioned GMRES algorithm. SIAM J. Sci. Comput. 1993; 14:461–469.

[54] Gumerov N.A., Duraiswami R. A broadband fast multipole accelerated boundary element method for the three dimensional Helmholtz equation. Journal of the Acoustical Society of America 2009; 125:191–205.

[55] Carpentieri B., Duff I., Giraud L., G. S. Combining fast multipole techniques and an approximate inverse preconditioner for large electromagnetism calculations. SIAM J. Sci. Comput. 2005;27(3):774–792.

[56] Niino K., Nishimura N. Preconditioning based on Calderon's formulae for periodic fast multipole methods for Helmholtz equation. Journal of Computational Physics 2012;231:66–81.

[57] Chaillat S., Semblat J., Bonnet M. A Preconditioned 3-D Multi-Region Fast Multipole Solver for Seismic Wave Propagation in Complex Geometries. Commun. Comput. Phys. 2012;11(2):594–609.